Key Points:
- Shallow pressure coring and MeBo drilling in a deepwater pockmark off Nigeria revealed gas hydrate saturations of up to 51% of pore space
- Shallow hydrates are fueled by thermogenic hydrocarbons mixed with microbial methane from petroleum degradation and from carbonate reduction
- Modeling of pore water chloride and sulfate independently suggests that last major methane injection event occurred during the past three centuries

Supporting Information:
- Supporting Information S1
- Movie S1

Correspondence to:
T. Pape,
tpape@marum.de

Shallow Gas Hydrate Accumulations at a Nigerian Deepwater Pockmark—Quantities and Dynamics

Thomas Pape[1] [iD], Livio Ruffine[2] [iD], Wei-Li Hong[3,4,5] [iD], Nabil Sultan[2] [iD], Vincent Riboulot[2] [iD], Carl A. Peters[1,6] [iD], Martin Kölling[1] [iD], Matthias Zabel[1] [iD], Sébastien Garziglia[2] [iD], and Gerhard Bohrmann[1] [iD]

[1]MARUM – Center for Marine Environmental Sciences, University of Bremen, Bremen, Germany, [2]IFREMER, Département Ressources physiques et Ecosystèmes de fond de Mer (REM), Unité des Géosciences Marines, Plouzané, France, [3]CAGE – Centre for Arctic Gas Hydrate, Environment and Climate, Department of Geology, UiT The Arctic University of Norway, Tromsø, Norway, [4]Marine Geology, Geological Survey of Norway, Trondheim, Norway, [5]Now at Department of Geological Sciences, Stockholm University, Stockholm, Sweden, [6]Ocean Frontier Institute, Dalhousie University, Halifax, Nova Scotia, Canada

Abstract The evolution of submarine pockmarks is often related to the ascent of fluid from the subsurface. For pockmarks located within the gas hydrate stability zone, methane oversaturation can result in the formation of gas hydrates in the sediment. An ~600 m-wide sea floor depression in deep waters offshore Nigeria, Pockmark A, was investigated for distributions and quantities of shallow gas hydrates, origins of hydrocarbons, and time elapsed since the last major fluid ascent event. For the first time, pressure coring of shallow sediments and drilling of more than 50 m-long cores with the sea floor drill rig MARUM-MeBo70 were conducted in this pockmark. Unusually, high hydrate saturations of up to 51% of pore volume in the uppermost 2.5 m of sediment in the pockmark center substantiate that deepwater pockmarks are a relevant methane reservoir. Molecular and stable C and H isotopic compositions suggest that thermogenic hydrocarbons and secondary microbial methane resulting from petroleum biodegradation are injected into shallower sediments and mixed with primary microbial hydrocarbons. Two independent pore water chloride and sulfate modeling approaches suggest that a major methane migration event occurred during the past one to three centuries. A rough sea floor topography within the pockmark most likely results from combined sediment removal through ascending gas bubbles, hydrate clogging and deflection of migration pathways, gas pressure build-up, and hydrate sea floor detachment. This study shows for the first time the chronological interrelationship between gas migration events, hydrate formation, and sea floor shaping in a deep sea pockmark.

1. Introduction

Pockmarks are (sub)circular to elliptical sea floor depressions that are known from shallow to deepwater areas worldwide. They exhibit a large variety of diameters (tens to thousands of meters) and sea floor morphologies. The evolution of pockmarks was attributed to various mechanisms including intense focused migration of fluids from greater depth and their subsequent escape at the seabed (Gay et al., 2007; Judd & Hovland, 2007; Paull et al., 1995) resulting in reduced sedimentation above sites of active seepage (Pau et al., 2014). Indeed, a great portion of pockmarks is characterized by high gas contents in shallow deposits, and seabed gas emissions were reported (e.g., Bünz et al., 2012; Judd & Hovland, 2007; Kelley et al., 1994; Marcon et al., 2014; Wenau et al., 2017). For deep sea gas-bearing pockmarks within the gas hydrate stability zone (GHSZ), occurrences of gas hydrates at shallow sediment depths are indicative for strong upward fluid migration sufficient to induce gas oversaturation in the pore water (e.g., Pape et al., 2020; Paull et al., 1995; Sahling et al., 2008). However, up to now only a few studies focused on the chronology of pockmark formation and temporal evolution (e.g., Chen et al., 2010; Luo et al., 2015; Pau et al., 2014; Sultan et al., 2014).

Pockmark A investigated in this study is located offshore Nigeria (Figure 1a) in a deepwater region that is known to host significant hydrocarbon reservoirs, which sustain gas hydrate formation in shallow sediments and potentially gas discharge from the sea floor. It belongs to a field of pockmarks that was intensively studied since 2004 for its subbottom structure in high-resolution, gas hydrate distributions, sea floor morphology, and evolution over time (George & Cauquil, 2007; Marsset et al., 2018; Sultan et al., 2010, 2014; Taleb
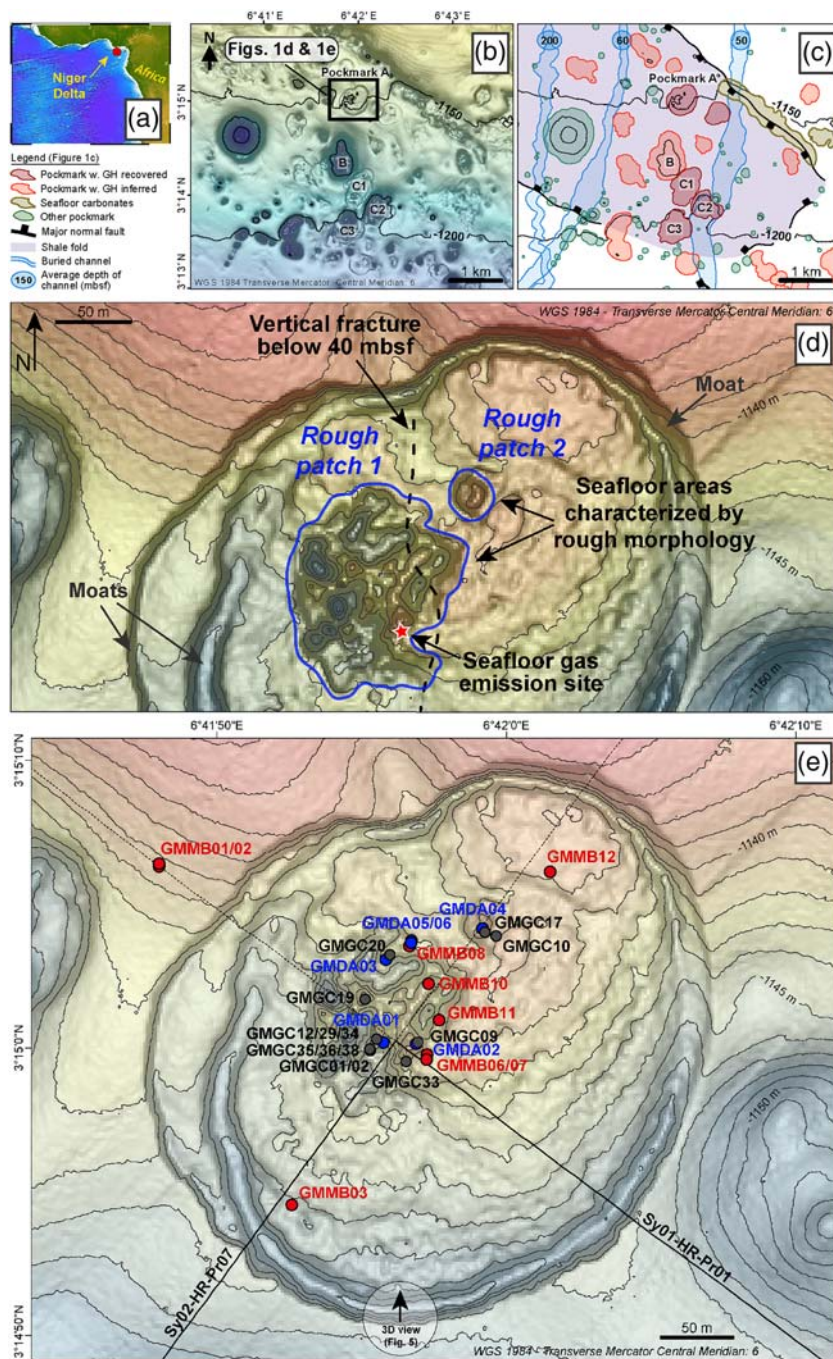
Figure 1. (a) Location of the pockmark field at the Nigerian continental margin comprising Pockmark A investigated in this study. (b) Shaded bathymetric map in the region of the pockmark field showing different pockmark shapes and sizes. In previous studies individual pockmarks have been investigated in detail by Bayon et al. (2007; Pockmark A), Sultan et al. (2010, 2014, Pockmarks A, B, C1, C2, and C3), Wei et al. (2015; Pockmarks A, C1, and C2), de Prunelé (2017; Pockmarks B, C1, C2, and C3), and Taleb et al. (2020; Pockmarks A and C2) for instance. (c) Positions of pockmarks, buried channels, and major normal faults projected on a bathymetric map of the study area (adopted from Sultan et al., 2014). The pockmark field is underlain by two NW-SE trending deep-rooted normal faults and N-S trending buried channels. "Other pockmarks": giant pockmarks, pockmarks related to fault systems or buried channels, other small-scale pockmarks that are likely not associated with deep-rooted acoustic chimney. (d) Bathymetric map of Pockmark A. Stippled black line indicates the sea floor projection of a prominent N-S-trending fracture identifiable in 3-D-seismic data below approximately 40 mbsf (see Sultan et al., 2010, 2014). Projection of sea floor position of gas emissions from Sultan et al. (2014). (e) Positions of MeBo cores (code GMMB; red), gravity cores (code GMGC; black), and pressure cores (GMDA; blue) as well as orientation of SYSIF seismic profiles Sy01-HR-Pr01 (NW-SE) and Sy02-HR-Pr07 (SW-NE) (Sultan et al., 2010).

et al., 2018). Individual pockmarks within this field were assumed to represent different stages in a multistep gas hydrate-related process affecting the sea floor morphology. Pockmark A is an erosive feature that was classified as active in terms of gas ascent in the recent past (Sultan et al., 2014) and proposed to typify an intermediate phase of the sea floor depression forming process (Sultan et al., 2010). Therefore, it provides excellent opportunities to determine quantities of pockmark-associated gas hydrates, evaluate hydrocarbon sources, elaborate time estimates for fluid upward migration events, and assess gas and hydrate-related factors shaping the seabed.

For the field of pockmarks, which also comprises Pockmark A, Sultan et al. (2010) proposed dissolution of shallow gas hydrates during phases of reduced fluid ascent to promote the creation of pockmark-related sea floor depressions. However, in order to evaluate the specific impact of shallow gas hydrates on pockmark evolution and seabed morphology, knowledge of their distributions and exact quantities is critical. One of several methods to quantify gas hydrates is pressure coring (e.g., Abegg et al., 2008; Pape et al., 2010; Pape et al., 2011a; Pape et al., 2011b; Pape et al., 2020), which has not been established for pockmarks yet.

Pore water chemistry is typically used for the characterization of fluid migration dynamics and gas hydrate formation in hydrocarbon-rich settings. Sediments above and adjacent to hydrates comprise the sulfate-methane interface (SMI) where sea water-derived sulfate is mostly consumed via the microbially mediated anaerobic oxidation of methane (AOM) (Boetius et al., 2000; Hoehler et al., 1994; Reeburgh, 1976). The depth of the SMI was often taken to delineate the methane-free sedimentary zone and to constrain the methane flux in the sediment column (e.g., Bhatnagar et al., 2008; Borowski et al., 1996; Dickens, 2001). Furthermore, chloride concentration anomalies are useful to track the evolution of hydrate formations (e.g., Peszynska et al., 2016; Torres et al., 2004, Torres et al., 2011), since ion exclusion during hydrate formation leads to chloride enrichments in the residual pore water (Ussler & Paull, 1995; Ussler & Paull, 2001).

Here we report on saturations of shallow gas hydrates deduced from shallow pressure coring at Pockmark A and discuss hydrate-related mechanisms affecting its sea floor morphology. Methane injection rates, time scales for hydrate formation, and evolution of the SMI were estimated by independently modeling the distributions of pore water chloride and sulfate in up to 57 m-long cores collected with the robotic sea floor drill rig MARUM-MeBo70 (Freudenthal & Wefer, 2013). A synoptic interpretation of these data from different methods enabled to provide a comprehensive picture on the interplay between last fluid migration events, gas hydrate formation and general evolution of developed hydrate-bearing pockmarks.

2. Geological Setting

The study area is located on the West African margin continental slope off Nigeria (Figure 1a) in the transitional detachment zone of the Niger Delta (Corredor et al., 2005; Rouby et al., 2011). The area is comprising a subcircular depression, called Pockmark A (N-S extension ~590 m; W-E ~490 m; Figures 1b–1e). It is delineated by two NW–SE trending deep-rooted normal faults that bound a graben, and two N-S trending channels buried at about 50–60 m below sea floor (mbsf) (Figure 1c; Bayon et al., 2007; Sultan et al., 2014). Minimum distances of the normal faults and the buried channels to Pockmark A are about 250 and 600 m, respectively.

Pockmark A is situated at water depths between 1,140 and 1,160 m below sea level (mbsl) and belongs to a pockmark cluster comprising individual negative sea floor reliefs and pockmark groups forming composite depressions (Sultan et al., 2010). It is separated from the surrounding seabed by a subcircular ring depression ("moat"), which at the western rim is partitioned into two separate but interconnected moats. Formation of the moat was related to hydrate dissolution and sediment collapse at the edges of the gas hydrate occurrence zone (GHOZ) (Riboulot et al., 2016; Sultan et al., 2010). Although generally flat-topped, Pockmark A comprises two restricted rough sea floor areas (called "Rough Patch 1" and "Rough Patch 2" hereafter) in its central and northern part (Figure 1d). These two patches ("Rough Patch 1": ~22,800 m^2; "Rough Patch 2": ~1,350 m^2) constitute about 11% of the total sea floor area that encloses the inner depression (~220,400 m^2). In particular, the sea floor along the western edge of the larger "Rough Patch 1" resembles an assemblage of pits each tens of meters in diameter and several meters in depth. Long sediment cores retrieved in 2011 with the sea floor drill rig MARUM-MeBo70 from the center and the periphery of Pockmark A predominantly contained homogeneous clay (Wei et al., 2015).

The morphology shaping the pockmarks in this area was explained by rapid hydrate formation in shallow sediments followed by slow dissolution (Sultan et al., 2010, 2014). At the two rough patches intense sea floor backscatter was observed in 2004 (George & Cauquil, 2007), indicating high concentrations of near-surface gas, gas hydrates, or methane-derived carbonates (Carson et al., 1994; Clague et al., 2001). A specific seismic reflector at about 230 mbsf was interpreted as a gas-charged body/"intermediate gas reservoir" ("horizon R"), which likely supplies free methane gas to the upper sedimentary layers through fractures within Pockmark A and the other adjacent pockmark-like structures (Sultan et al., 2010, 2014; Taleb et al., 2020). At Pockmark A, a prominent N-S trending fracture crosses the central part of the depression (Figure 1d). High-amplitude reflectors on seismic profiles were interpreted to indicate the presence of free gas and gas hydrates in a sedimentary zone close to the sea floor at the two rough patches (Sultan et al., 2014). Natural sea floor gas emissions demonstrating fluid upward migration were discovered from a site at "Rough Patch 1" close to the central fracture in 2011 (Figure 1d) (Sultan et al., 2014). The presence of abundant authigenic aragonite in surface sediments was interpreted to result from intense AOM in the course of past seepage events (Fontanier et al., 2014) and attests for past shallow methane migration within the depression.

In Pockmark A, gas hydrates are widely distributed in a sediment body down to a depth of 34 mbsf at maximum (Sultan et al., 2014; Taleb et al., 2018, 2020; Wei et al., 2015). Gas hydrates with gas-filled macropores in shallow sediments of the "Rough Patch 1" (Sultan et al., 2014) point to their rapid formation from gaseous methane (e.g., Bohrmann et al., 1998; Torres et al., 2004).

Furthermore, relatively steep temperature gradients exceeding 198°C km^{-1} were measured in the topmost 3.5 m of sediment at two sites between the two rough patches in 2011 (Wei et al., 2015). These gradients in the central part of Pockmark A are localized and much higher than the gradients measured close to the NW rim (~80°C km^{-1}; Sultan et al., 2010; Wei et al., 2015); outside the pockmark (72°C km^{-1}; Wei et al., 2015) and the majority of measurements obtained elsewhere on the Nigerian continental slope (Brooks et al., 2000). In Pockmark A gradients are spatially highly variable and likely caused by localized upward migration of hot fluids (Wei et al., 2015). Local sediment temperature variations, although to a lower extent, may also result from hydrate formation and dissociation that affect the thermal properties of the bulk sediment (Waite et al., 2007). For shallow sediments at a station at the southeastern rim of the pockmark, Sultan et al. (2014) related localized positive temperature anomalies to recent hydrate formation induced by free gas flux trough fractures. Using linear interpolation with depth, Wei et al. (2015) calculated positions of the base of the GHSZ (BGHSZ) for structure I (sI) hydrates ranging between ~130 mbsf (72°C km^{-1}) in the outer parts of the Pockmark and at the border of "Rough Patch 1" and 35 mbsf (258°C km^{-1}) for stations located between the two rough patches.

3. Data and Methods

Data and samples from Pockmark A (Figure 1) were acquired during a cruise with RV "Pourquoi pas?" in the frame of the joint French-German GUINECO-MeBo project in November/December 2011.

3.1. Subsurface Data Acquisition

Very high resolution 2-D seismic data along profiles Sy01-HR-Pr01 and Sy02-HR-Pr07 (Sultan et al., 2010) were acquired during the ERIG3D cruise in 2008 using the deep-towed SYSIF (Système Sismique Fond) that provides images of the uppermost ~75 m of sediments (100 ms two way travel time, twtt, below sea floor) with resolutions of about 0.3 m in vertical and 6 m in horizontal direction (Ker et al., 2010; Marsset et al., 2010). The resulting subsurface data were considered to define positions of coring sites investigated herein and in particular at sites where shallow gas hydrates were suspected.

3.2. Sampling and Sample Preparation

Six pressure cores of shallow sediments (down to 2.65 mbsf) were taken with the Dynamic Autoclave Piston Corer (Abegg et al., 2008; DAPC, core code GMDA) at five sites in the two rough patches (George & Cauquil, 2007) where preceding gravity and MeBo cores documented the presence of shallow gas hydrates (Figures 1 and 2; Table 1). Unpressurized sediment cores of up to 56.7 m in length were recovered with the sea floor drill rig MARUM-MeBo70 (Freudenthal & Wefer, 2013) (core codes GMMB). These were amended by cores obtained with a conventional gravity corer (core code GMGC). It should be noted that
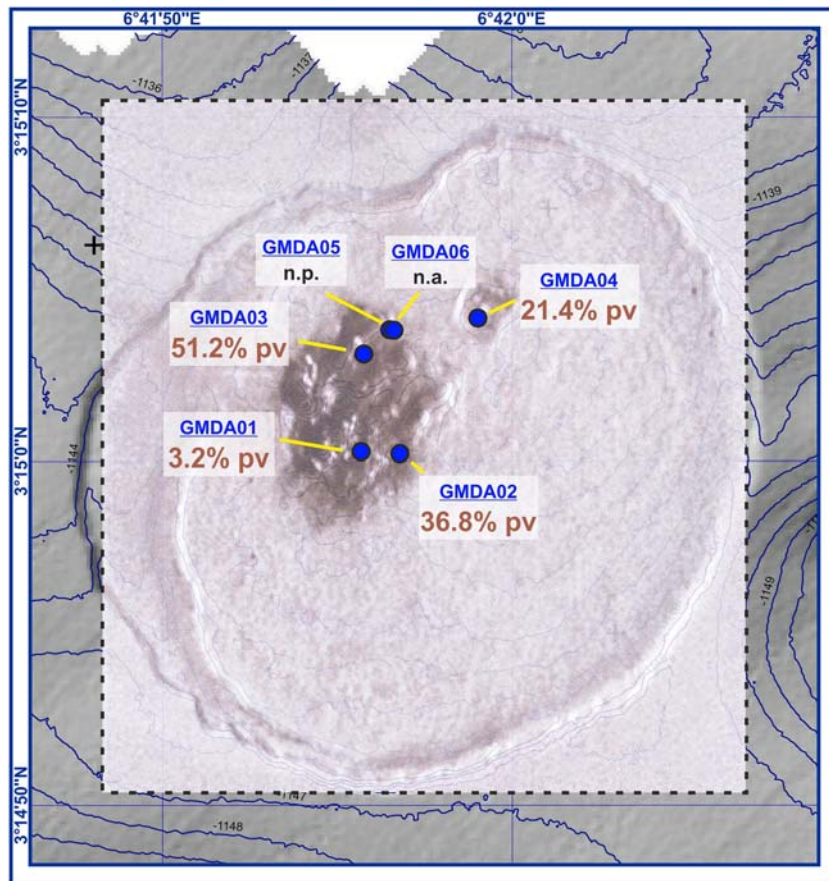
Figure 2. Sea floor backscatter map (George & Cauquil, 2007) overlaid on bathymetric map as well as positions and hydrate saturations (in % pore volume) in pressure cores taken with the Dynamic Autoclave Piston Corer. n.p. = not present, n.a. = not analyzed.

lowering, placement on the sea bed, and initial sinking of the MeBo system have caused disturbance and likely removal of the uppermost decimeters of unconsolidated sediments. Top sediments have probably also been lost during recovery of the gravity cores. Because sediment loss has not been determined in this study, we consider reported sediment depths as minimum depths.

For vertical profiling of ex situ methane concentrations in the nonpressurized MeBo cores, headspace gas samples were prepared immediately after recovery according to the technique designed by Kvenvolden and McDonald (1986) in a modified version described in Pape et al. (2014). Three milliliters of sediment was taken with cut-off syringes shortly after core recovery, when concentrations of light hydrocarbons have still not equilibrated to ambient pressure, at defined depths and transferred into 20 ml glass vials prefilled with 5 ml of 1 M NaOH for storage until analysis of methane concentrations in the headspace gas on board.

Hydrate-bound gas was collected from hydrate pieces according to Pape et al. (2010) and transferred into glass serum vials prefilled with saturated NaCl solution for on-board analysis of molecular compositions and for storage until determination of methane stable carbon and hydrogen isotope compositions onshore.

For quantification of total gas volumes and hydrate saturations, the DAPC cores were degassed onboard incrementally under controlled conditions as described in Pape et al. (2011b). Total gas volumes stated are the cumulative amounts of all gas and sediment-water slurries that were supplied from the pressurized core as determined at ambient pressure. At selected pressure stages, gas subsamples were taken from the released gas and transferred into glass serum vials prefilled with saturated NaCl solution for storage until analysis.

Pore water was extracted from selected sediment depths ex situ at 4°C with Rhizon soil moisture samplers (Seeberg-Elverfeldt et al., 2005) from MeBo cores and gravity cores after removal of gas hydrate pieces,

Table 1
Overview of Sediment Cores Retrieved During Cruise Guineco-MeBo 2011 From Pockmark A and Considered in This Study

Internal core code (cruise) GMXX-XX	Supplementary core code ("Pangaea") GeoB160XX-XX	Water depth (mbsl)	Sampled area	Core recovery (m)	Sulfate penetration depth/ToGH (m)	Comment
Pressure cores						
GMDA01	16009-1	n.doc.	Patch 1	1.75	0.30/n.det.	
GMDA02	16014-1	n.doc.	Patch 1	0.67	0.50/n.det.	
GMDA03	16027-1	n.doc.	Patch 1	0.97	0.30/n.det.	
GMDA04	16029-1	1,143	Patch 2	2.36	0.50/n.det.	
GMDA05	16032-1	1,145	Patch 1	2.44	1.25/n.det.	
GMDA06	16050-1	1,145	Patch 1	2.05	n.anal./n.det.	
Gravity cores						
GMGC01	16001-1	n.doc.	Patch 1	2.00	0.65/1.10	
GMGC02	16001-2	n.doc.	Patch 1	1.10	n.anal./0.85	
GMGC09	16011-1	n.doc.	Patch 1	2.40	n.anal./1.00	
GMGC10	16012-1	n.doc.	Patch 2	2.20	0.65/0.80	
GMGC12	16013-2	n.doc.	Patch 1	n.doc.	n.anal./n.det.	
GMGC17	16022-1	n.doc.	Patch 2	3.50	n.anal./3.20	
GMGC19	16024-1	n.doc.	Patch 1	1.10	n.anal./0.85	
GMGC20	16025-1	n.doc.	Patch 1	2.90	n.anal./0.65	
GMGC29	16041-1	1,144	Patch 1	core barrel empty, only cc	n.pres./n.pres.	
GMGC33	16045-1	1,147	Patch 1	1.00	n.anal./0.60	
GMGC34	16046-1	1,143	Patch 1	1.80	n.anal./0.60	
GMGC35	16046-2	1,143	Patch 1	3.20	n.anal./0.70	
GMGC36	16046-3	1,143	Patch 1	n.doc.	n.anal./n.det.	
GMGC38	16046-4	1,143	Patch 1	n.doc.	n.anal./n.det.	
MeBo cores						
GMMB01/−02	16002-1/16003-1	1,141	outside sea floor depression	53.30	40.42/n.det.	Sultan et al. (2014); Wei et al. (2015)
GMMB03	16010-1	1,148	SW rim	45.18	4.30/6.95	Sultan et al. (2014); Wei et al. (2015)
GMMB06	16021-1	1,148	Patch 1	6.74	2.50/3.40	Sultan et al. (2014); Wei et al. (2015)
GMMB07	16028-1	1,148	Patch 1	10.19	2.00/2.85	Sultan et al. (2014); Wei et al. (2015)
GMMB08	16030-1	1,142	Patch 1	56.84	n.det./5.35	Sultan et al. (2014); Wei et al. (2015)
GMMB10	16036-1	1,142	Patch 1	23.95	1.52/5.15	Sultan et al. (2014); Wei et al. (2015); discharge of free gas during drilling
GMMB11	16042-1	1,146	Patch 1	12.57	n.det./6.65	Sultan et al. (2014); Wei et al. (2015); discharge of free gas during drilling
GMMB12	16049-1	1,144	NE rim	24.75	4.20/7.26	Sultan et al. (2014); Wei et al. (2015)

Note. For sampling locations see Figure 1e. Additional specifics of MeBo cores can be found in the database of "Pangaea" = PANGAEA – Data Publisher for Earth & Environmental Science (https://www.pangaea.de/). ToGH = Top of Gas Hydrates. Patch 1/2 = "Rough Patch 1" or "2"; n.doc. = not documented; n.det. = not determined; n.anal. = not analyzed; n.pres. = not present; cc = core catcher.

and from DAPC cores after degassing. Dissociation of small, overlooked gas hydrates that remained in the sediments may have caused partial dilution of pore water samples from the GHOZ. Therefore, reported positive anomalies in chloride concentrations existing in situ might have been higher than those measured. This indeterminable error has contributed to an increase in the total analytical error inherent in the preparative and analytical method.

3.3. Sample Analysis

All nonpressurized cores were cut in meter segments, which were analyzed using a Multi-Sensor Core Logger (MSCL) from Geotek® to determine gamma-density profiles. This property was used to derive porosity for the geochemical modeling by considering a density of 2.65 g ml^{-1} for the sediment and 1.030 g ml^{-1} for the pore water.

Gas samples were analyzed onboard for their molecular compositions and methane concentrations by gas chromatography (GC) (Pape et al., 2010). Concentrations of dissolved methane stated are ex situ concentrations uncorrected for sediment porosity and Bunsen coefficient. Stable carbon and hydrogen isotope ratios

(^{13}C/^{12}C; ^{2}H/^{1}H) of CH$_4$ in hydrate-bound gas were determined at MARUM by GC-isotope ratio mass spectrometry (GC-IRMS). Carbon and hydrogen isotopic ratios are reported in δ-notation in parts per mil relative to the Vienna PeeDee Belemnite (V-PDB) and Standard Mean Ocean Water (V-SMOW), respectively. Standard deviations of triplicate stable isotope measurements were <0.5‰ (δ^{13}C-CH$_4$) and <1.5‰ (δ^{2}H-CH$_4$).

Pore water analysis was done on board shortly after extraction. Concentrations of chloride (Cl$^-$) and sulfate (SO$_4^{2-}$) were determined by ion chromatography (Metrohm, 861 Advanced Compact IC). Standard sea water from the International Association for Physical Sciences of Oceans (IAPSO) was used for calibrating the system. The analytical error for concentrations was estimated at ±3%. Sulfate was frequently found in concentrations > 1 mM in MeBo cores below the inferred depth of the SMI (Figures 3a and 3b). This was unlike observations in long piston cores retrieved during the same expedition with the IFREMER Calypso piston corer that also penetrated the SMI (data not shown in this study). This observation was restricted to MeBo cores and can be ascribed to the intrusion of bottom sea water that was used as flushing fluid during MeBo drilling operations (Freudenthal & Wefer, 2013); an interpretation also proposed in earlier studies (Orcutt et al., 2017; Wallmann et al., 2018; Wei et al., 2015). Thus, the virtual absence of sulfate below the SMI under in situ conditions (conc. = 0 mM) was assumed for the modeling approaches adopted in this study. For this, measured sulfate concentrations in samples from below the SMI were used to calculate the fraction of sea water that potentially has mixed up with pore water (see Wei et al., 2015; Wallmann et al., 2018) and to recalculate initial chloride concentrations in the pore water.

3.4. Calculations of Gas Hydrate Saturations in Pressure Cores

Total gas volumes from the six pressure cores were used to calculate true gas hydrate saturations (GHsat$_{tr}$) in shallow sediments according to Pape et al. (2011a). Briefly, total gas volumes released from pressure cores at ambient pressure were converted to methane amounts considering the molecular composition of hydrate-bound gas (section 4.2). Sulfate concentration profiles were used to evaluate core specific sulfate penetration depths; that is, sulfate zones virtually devoid of methane. Pore volumes in sediments below the sulfate penetration depth were calculated using bulk core volumes below the sulfate zone (at ambient pressure) and average porosities of 83%, as well as minimum (75%) and maximum (90%) porosities in sediments above ~5 mbsf (see Text S2 and Figure S2 in the supporting information). Integral methane concentrations (in mol dm^{-3}) were calculated by converting the cumulative volume of methane determined at ambient pressure and 20°C via the ideal gas law. The amount of methane in mole is referred to the average total pore volume inside the pressure core using a porosity of 83% (see above).

Core specific upper boundaries of GHOZs were assigned considering sediment textures (e.g., mousy/soupy sediment) as well as chloride and sulfate concentration profiles. Methane solubilities were determined according to either Duan and Mao (2006) (between depth of sulfate penetration and top of gas hydrates [ToGH]) or Tishchenko et al. (2005) (within the gas hydrate zone). The amounts of dissolved methane present above the ToGH and within the GHSZ were subtracted from total methane amounts in order to determine the mass of hydrate-bound methane. The amount of hydrate-bound methane was related to pore volume below the ToGH in order to calculate GHsat$_{tr}$ (in % pore volume). GHsat$_{tr}$ considering minimum (75%) and maximum (90%) sediment porosities differed by 12% at maximum from those calculated based on average porosities. In the following, GHsat$_{tr}$ obtained from average porosities are discussed.

3.5. Geochemical Modeling of Chloride and Sulfate Concentrations
3.5.1. Primary Principles for the Two Geochemical Modelings

Two transport-reaction models were used to independently simulate the profiles of dissolved chloride and sulfate and to determine the time scales of methane flux increase. Despite the similar overall mathematical architecture in both models, the simulations were done relying on entirely different principles and geochemical processes.

For the chloride model, we simulated the effect of gas hydrate dynamics on dissolved chloride concentration. Ion exclusion during hydrate formation results in enrichment of solutes, such as chloride, in the pore water (Ussler & Paull, 1995). In the case of halted or decreased rates of hydrate formation, excess chloride is gradually removed with progressing time by diffusion and/or fluid advection, which finally results in smooth concentration profiles without excess chloride. In contrast, excess chloride
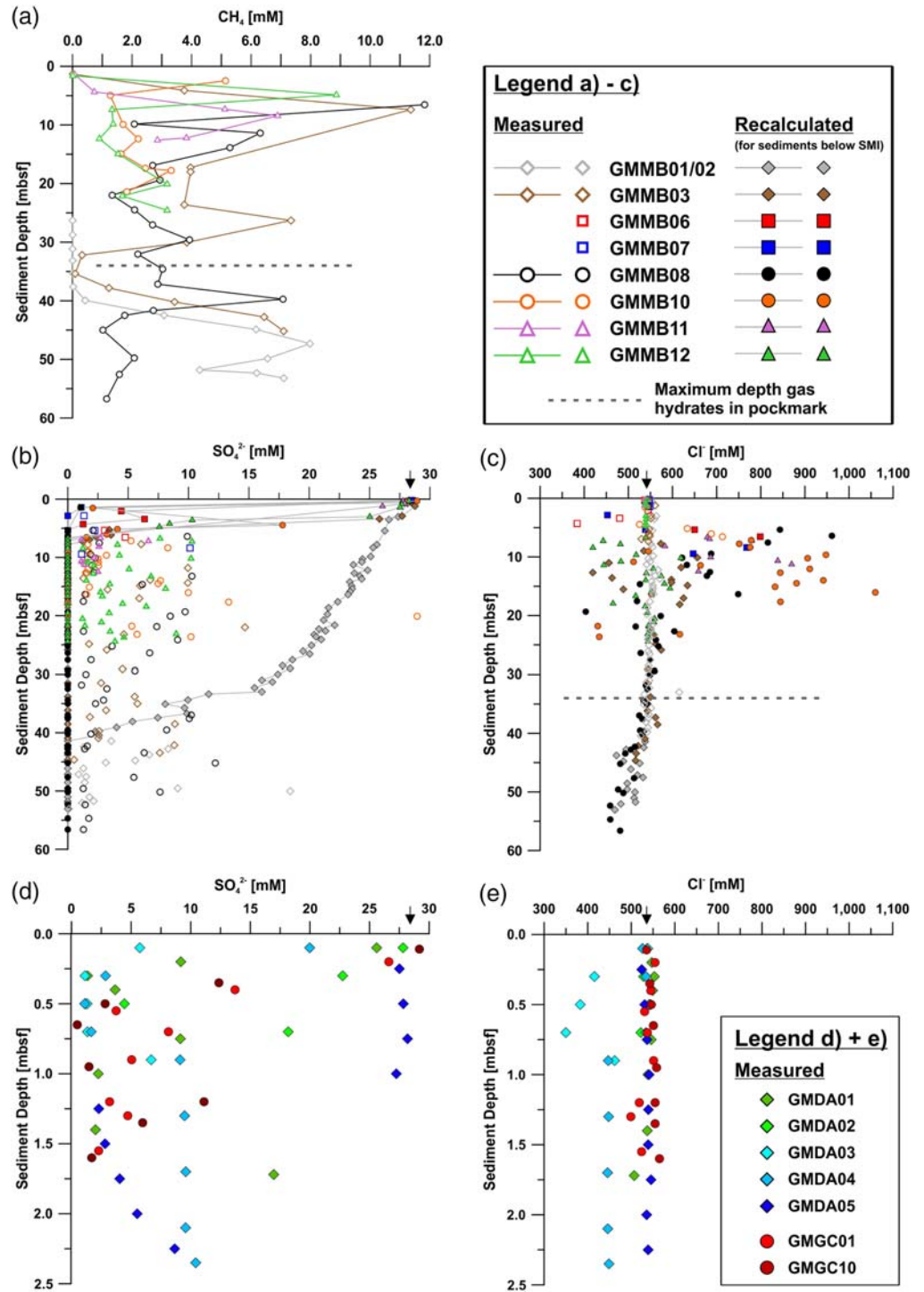
Figure 3. (a) Depth profile of measured ex situ methane concentrations in headspace gas extracted from sediment samples retrieved with MeBo. Note: gas samples not prepared from GMMB06 and GMMB07. Depth profiles of (b) measured (open symbols) and recalculated (closed symbols) pore water sulfate concentrations and (c) recalculated pore water chloride concentrations in MeBo cores. Recalculated pore water chloride concentrations adapted from Wei et al. (2015). Measured sulfate and chloride concentrations in MeBo cores GMMB01/02, GMMB06, and GMMB07 already reported in Sultan et al. (2016). Note: Black arrows on top axis for chloride and sulfate concentrations indicate typical bottom sea water concentrations. Depth profiles of (d) measured pore water sulfate concentrations and (e) measured pore water chloride concentrations in pressure cores and gravity cores. Stippled horizontal lines in (a) and (c) indicate the maximum depth of the gas hydrate occurrence zone (GHOZ) in Pockmark A as inferred from seismic data (~34 m; see Taleb et al., 2020).

concentrations are still preserved in recovered sediments if hydrate formation is faster than diffusion; that is, hydrate formation is the dominant process compared to ion diffusion. Enrichments in chloride concentrations have been observed in several settings of hydrate-bearing sediments and interpreted as indicator for methane transport in the gas phase and rapid hydrate formation (e.g., Haeckel et al., 2004; Peszynska et al., 2016; Torres et al., 2004, 2011). Therefore, the profile with excess chloride concentration can be used to assess the time scales of hydrate formation in response to the methane pulse within the sediment.

For the sulfate model, the simulation primarily focuses on the rate of sulfate consumption as a result of increasing methane supply. At locations where large methane fluxes are observed, most of sulfate consumption is tied to methane consumption through AOM (Boetius et al., 2000). If sulfate consumption through AOM is comparable to the diffusional supply of sulfate from the bottom sea water, a smooth sulfate pore fluid profile illustrating a steady-state system is expected. On the other hand, dissolved sulfate profiles with distinct kinks (e.g., in Figure 3b) were observed at a few locations indicating recent and sudden changes in methane supply (Fischer et al., 2013; Hensen et al., 2003; Hong et al., 2017). A large pulse of methane stimulates abnormally high AOM rate, which consumes sulfate faster than its seawater replenishment. The sulfate profiles below the kinks reflect such anomalously high sulfate consumption whereas the profile above has not yet been affected by the changes in methane supply. By simulating such bended sulfate profiles, the timing of increasing methane supply can be estimated, as done in previous studies (Fischer et al., 2013; Hong et al., 2017).

The model-derived time scales are therefore constrained by independent processes. A comparison of the results can provide insights into the methane seepage history as the chloride modeling is based on physical phase change during hydrate formation, while the sulfate modeling considers biogeochemical transformation of methane during the AOM. It is also important to note that, though a methane supply is assumed in both models, the causes of increasing methane seepage cannot be determined by either model and are beyond the scope of this study.

In order to evaluate uncertainties for the time scales resulting from the different porosity values, a dimension analysis was conducted using the observed range of porosity. This analysis showed that a decrease in porosity by 15% (90% to 75%) leads to a 1.3-fold increase of time required for diffusion. This factor is considered as the uncertainty for the time scales estimated herein.

3.5.2. Chloride Concentrations

In order to quantify the time scale of gas hydrate formation at Pockmark A, a 1-D transport-reaction model developed by Peszynska et al. (2016) and later tested by Hong and Peszynska (2018) was applied. The model considers ion diffusion and fluid advection of a system with two phases (water and solid) and three components (H_2O, methane, and NaCl). No gas phase is considered, and, thus, the model is only applicable to sediments above the BGHSZ. It is known that free methane gas can be present in the GHOZ despite the violation of thermodynamics principles (Daigle & Dugan, 2011; Flemings et al., 2003; Liu et al., 2019; Torres et al., 2004). Methane gas locked into gas hydrates within the GHOZ has also been observed within the macropores of gas hydrates recovered from GMGC12 within the "Rough Patch 1" (Sultan et al., 2014). However, the impact of the presence of free methane gas on the chloride diffusion in the pore space is considered insignificant as these two compounds do not react with each other.

The modeling approach adopted in this study does not include such likely transient occurrence of free methane gas and should be deemed as a simplified model. Precipitation or dissolution of gas hydrates is assumed to happen immediately in the model, when the conditions are satisfied; that is, no kinetic barriers exist. Therefore, the extent of methane solubility (MSol), a function of temperature, pressure, and salinity, is the only factor to determine hydrate dynamics. The local gas hydrate equilibrium (GHEQ) and MSol were derived by using the CSMGem program (Sloan & Koh, 2007) with information of temperature, pressure, and salinity from the investigated sites (see Text S1 and Figure S1).

Constant geothermal gradient within the time scale of interest is assumed for the investigated sites (see Table S2 for values used). Such assumption does not account for the variable thickness of hydrate stability as a result of fluctuating heat flow that likely occurred in Pockmark A (Wei et al., 2015). We, however, noted that much of the changes in chloride concentration occur in the top 30 m of sediments (Figure 3c). This depth interval is well within the GHSZ even at sites of highest geothermal gradient, that is, 258°C

km^{-1} as measured in the top 2.5 meters of sediments in the central part of Pockmark A. Therefore, the sediment depth covered by the model is consistently situated within the hydrate stability zone despite the varying geothermal gradient, and all assigned thermodynamic parameters are, thus, valid.

As pore water salinity has not been measured, salinity was related with pore water chloride concentration through an empirical relationship derived by Peszynska et al. (2016). The two parameters are, therefore, exchangeable in this study. MSol was derived to cover the chloride concentration from fresh water to those doubling the typical sea water concentration (~1,110 mM), a range that covers concentrations observed herein. Details about how GHEQ and MSol were derived are given in the supporting information.

For modeling the evolution of gas hydrates, recalculated pore water chloride concentrations from six MeBo cores at four different sites from the center to the pockmark rim were chosen: (a) GMMB03, (b) GMMB12, (c) GMMB10, and (d) GMMB06/07/11 (Figure 1e). Results from joint cores GMMB01/02 were not modeled, as no chloride enrichment was detected at this site (Figure 3c); instead, profiles from these cores were used to derive fluid advection rates and, additionally, served as the initial condition for the model. We focused on the uppermost 53 m of sediments for all sites except for Site GMMB10 (top 34 m of sediments only; see Figure 6), which was affected by a relatively high geothermal gradient ($\geq$119°C km^{-1}; Wei et al., 2015) and a shallower BGHSZ as compared to other investigated sites. Similar to the model setup reported in Torres et al. (2004) and Peszynska et al. (2016), in this study a constant methane source was added in the model from intermediate depths of the sediment column where the positive chloride concentrations were observed (Figure 6; usually between 3 and 18 mbsf; see Table S2 for exact depth range). The nature of the methane source is discussed in section 4.4.1. The basic parameters used in the model, such as model length, geothermal gradient, porosity, fluid advection rate, and boundary conditions, are summarized in Texts S2–S4 and Figures S2 and S3.

3.5.3. Sulfate Concentrations

The depth profiles of sulfate concentration indicate that in the shallow sediment of the pockmark, which is of relevance for this study, methane is supplied from the ToGH. This assessment is supported by the relatively short distance between the ToGH and the SMI (Table 1). Because lateral fluid migration was not observed in the interval between the ToGH and the SMI, the sulfate concentration profiles can be simulated by a 1-D transport-reaction model. This is in contrast with sediments below approximately 32 mbsf at Site GMMB01/02 outside Pockmark A, for which Sultan et al. (2016) considered lateral fluid advection due to the presence of distinct coarse-grained and, thus, highly permeable sediment layers and applied 2-D modeling. In this study, a 1-D numerical AOM-driven transport-reaction model was developed in gPROMS software (Process System Enterprise, PSE Ltd) to simulate the evolution of sulfate consumption by AOM with time:

$$\Phi\frac{\partial[C_i]}{\partial t} = \frac{\partial}{\partial x}\left[\Phi\frac{D_i}{\vartheta^2}\frac{\partial[C_i]}{\partial x}\right] - \Phi\upsilon\frac{\partial[C_i]}{\partial x} - \Phi R_{AOM}, \tag{1}$$

where t is the time (year), Φ is the sediment porosity, x is the depth within the sedimentary column (m), υ is the upward fluid velocity, ϑ is the sediment tortuosity, and C_i and D_i are the measured concentration (mM) and diffusion coefficient ($m^2\ year^{-1}$) of the dissolved species "i," respectively.

The model is derived from the diagenetic equations published by Berner (1980) and Boudreau (1997) and considers the transport of species by both diffusion and advection. As pointed out in section 2, earlier studies have shown that hydrate formation is rapid in the area, with a multilayered distribution within the sedimentary column (de Prunelé et al., 2017; Sultan et al., 2014). Thus, assuming that the upper hydrate layer is the methane source for the AOM reaction (de Prunelé et al., 2017) and considering a rapid hydrate formation process following sudden gas release, it is possible to estimate the time elapsed since this formation. The same values of the upward fluid velocity υ were tested for both models with the sulfate- and chloride-(enrichment)-related processes. It was checked with the chloride profiles by considering the sedimentary interval above the hydrate layer only, which was not disturbed by pore water freshening. Reduction of porosity upon hydrate formation is irrelevant for the model applied as geochemical processes occurring within the sedimentary interval bounded by the ToGH and the SMI only are considered.

Boudreau's empirical formulation (Boudreau, 1997) was taken for the calculation of the tortuosity:

$$\vartheta^2 = 1 - ln\left(\theta^2\right). \tag{2}$$

The AOM rate was expressed by the following kinetic equation:

$$R_{AOM} = k_{AOM}[SO_4][CH_4] \tag{3}$$

with k_{AOM} being the kinetic constant of the reaction. Methane concentration at the boundary domain was calculated from the online Duan's Research Group thermodynamics model (Sun & Duan, 2007). Basic parameters used in the model, such as model lengths, are summarized in Table S3.

4. Results

4.1. Sediment Composition and Texture

Sediment collected with MeBo cores, gravity cores, and pressure cores predominantly consisted of homogenous dark clay with occasionally abundant carbonate concretions. In some gravity cores and MeBo cores disseminated platy gas hydrates (less than ~2 cm in diameter) or even hydrate pieces of several cm in diameter (e.g., GMGC12 close to GMDA01; GMGC20 close to GMDA03), occasionally in comparably high concentration, were present in sediments deeper than approximately 65 cmbsf. In addition, hydrate pieces showing bubble fabrics were found in GMGC12 recovered from the "Rough Patch 1" (Sultan et al., 2014).

Specific sediment intervals (up to about 33 cmbsf for instance in GMGC33 close to GMDA02) were fluidized (moussy/soupy textures) as a result of gas hydrate dissociation and/or injection of free gas from deeper core parts during recovery of the unpressurized cores (Table S1). Hydrate dissociation was initiated by pressure decrease and/or temperature increase during retrieval of the gravity and MeBo cores through the temperate water column. Although not investigated in detail in this study, the depth distribution of fluidized sediments correlated with pore water chloride concentration anomalies in general.

4.2. Gas Hydrate Saturations in Pressure Cores, Vertical Methane Distributions, and Hydrocarbon Chemistry

Volumetric gas-bulk sediment ratios determined from the degassing of the six DAPC cores at ambient pressure ranged between 0.4 and 54.4 (L L^{-1}; Table 2). Assuming hydrate sI to prevail (see hydrocarbon chemistry below), integral hydrate saturations (GHsat$_{tr}$) in the core interval between the base of the sulfate zone (see section 4.3) and the maximum penetration depth of the DAPC (244 cm) were highest in core GMDA03 (51.2% per pore volume (pv); Table 2; Figure 2). This core and core GMDA02 (GHsat$_{tr}$ = 36.8% pv) were recovered from "Rough Patch 1". Comparably, high GHsat$_{tr}$ (16.9% pv) was also measured in core GMDA04 from "Rough Patch 2". In contrast, volumes of gas released from GMDA05 and GMDA06 taken at the northern border of "Rough Patch 1" were below the methane saturation threshold under in situ conditions, thus indicating the absence of gas hydrates in these cores.

Sedimentary gas (headspace analysis) from depressurized MeBo cores that have experienced degassing during recovery and core handling contained concentrations of dissolved methane approaching the lower millimolar-range (Figure 3a). Maximum methane concentrations (of >11.8 mmol L^{-1}) were found in GMMB08, which was drilled at the northern boundary of the "Rough Patch 1" (Figures 1d and 1e), at 6.55 mbsf and may be explained by the presence of small, undetected hydrate crystals in the sample. This MeBo core was located close to pressure cores GMDA05 and GMDA06 that did not document the presence of gas hydrates in shallow sediments. Other drill sites close to the pockmark rim (GMMB03 and GMMB12) showed methane concentrations similar to those detected in the center of the pockmark (GMMB08, GMMB10, and GMMB11). In the 53.3 m-long core drilled NW off the pockmark center (GMMB01/02), methane enrichments of up to 8.0 mmol L^{-1} were found below approximately 38 mbsf. In general, methane concentration profiles showed several peaks with shallowest maxima between ~2.5 and 20 mbsf.

Molecular hydrocarbon ratios (C$_1$/C$_{2+}$) in hydrate-bound gas ranged between ~3,050 and 23,800 ($n = 21$; Figure 4a; Table S4). No clear relation between the position of sampling sites and C$_1$/C$_{2+}$ ratios became apparent. δ^{13}C-CH$_4$ values ranged between −53.4‰ and −49.4‰, and δ^2H-CH$_4$ plotted between −182.9‰ and −178.3‰ (Figure 4b; Table S4). Methane in relatively deeply buried hydrates retrieved with MeBo

Table 2
Accumulated Gas Volumes, Gas-Sediment Ratios (at Ambient Pressure), Methane Concentrations (Average Porosity 83%), and Calculated Fractions of sI Hydrates in Sediment Cores Recovered by Pressure Coring (GHsat_{tr})

DAPC core code	Core recovery (m)	Total gas volume release d(L)	Volumetric gas-sediment ratio (total core) (L L^{-1})	Conc. CH$_4$ (total core) (mol dm^{-3})	Core volume below sulfate zone (L)	Hydrate saturation (sI) in pore volume below sulfate zone (GHsat$_{tr}$) (%)	Model-derived hydrate saturation (GHsat$_{mod}$) (%)
GMDA01	1.75	52.62	5.63	0.28	7.75	3.2	
GMDA02	0.73	59.15	16.52	0.83	0.91	36.8	38[a]
GMDA03	1.04	282.15	54.44	2.73	3.58	51.2	46[b]
GMDA04	2.36	342.90	27.19	1.36	9.94	21.4	11[c]
GMDA05	2.44	4.82	0.37	0.02	6.36	n.p.	
GMDA06	2.05	4.10	0.37	0.02	n.a.	n.a.	
					average	31.4 ($n = 4$)	

Note. Model-derived gas hydrate saturations (GHsat$_{mod}$) at MeBo drill sites are included. n.p. = not present; n.a. = not analyzed.
[a]GMMB06, GMMB07, and GMMB11.   [b]GMMB10.   [c]GMMB12.

appeared to be slightly less depleted in ^{12}C compared to that in their shallow counterparts collected with the gravity corer. No similar trend was apparent in δD-signatures of hydrate-bound methane.

4.3. Pore Water Geochemistry

Concentrations of pore water sulfate and chloride were investigated as indicators of upward methane flux intensities and markers of the evolution of the gas hydrate system. Chloride concentrations in all MeBo cores as well as sulfate concentrations in MeBo cores GMMB01/02 and GMMB05 (Figures 3b and 3c) were already reported in previous studies (Sultan et al., 2014, 2016; Wei et al., 2015).

In gravity cores and pressure cores sea water-derived sulfate was found in sediments as deep as about 3.2 mbsf (e.g., GMGC17; Table 1). In general, shallowest positions of the SMI (0.30–0.65 mbsf) were found in the pockmark center (Figure 3b; Table S1), where seismic data and MeBo drilling indicated the shallowest ToGH (Figure 5). Deep pore water samples from core GMMB08 suggested that ascending fluids are generally sulfate-free. Those samples additionally showed that ascending fluids are only slightly depleted in Cl$^-$
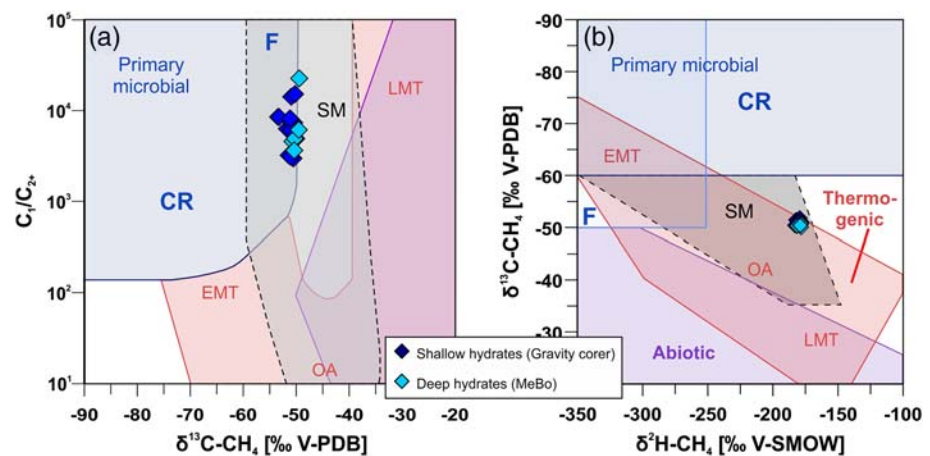

Figure 4. Genetic diagrams for hydrocarbon sources below Pockmark A. (a) "Bernard diagram" modified after Milkov and Etiope (2018) showing δ^{13}C values of methane versus molecular hydrocarbon ratios (C$_1$/C$_{2+}$) for hydrate-bound methane collected from Pockmark A. All samples plot in the fields assigned for microbial and thermocatalytic hydrocarbons close to the field representative for secondary microbial hydrocarbons (SM). In general, methane bound in deep hydrates (greater than ~7.4 mbsf) is slightly less depleted in ^{12}C compared to that bound in shallow hydrates (less than ~3.5 mbsf). Note: In a previous study, a C$_1$/C$_2$ ratios of 1,720 was determined for hydrocarbons in headspace gas prepared from the base of the "gas hydrated core" NCG102 from our study area (Brooks et al., 2000). (b) Crossplot of δ^{13}C values versus δ^{2}H values of methane in selected samples of hydrate-bound methane (classification adopted from Milkov and Etiope (2018)). The samples plot within the fields assigned for thermogenic and secondary microbial hydrocarbons. CR = carbonate reduction; F = methyl-type fermentation; EMT = early mature thermogenic gas; SM = secondary microbial; OA = oil-associated thermogenic gas; LMT = late mature thermogenic gas.
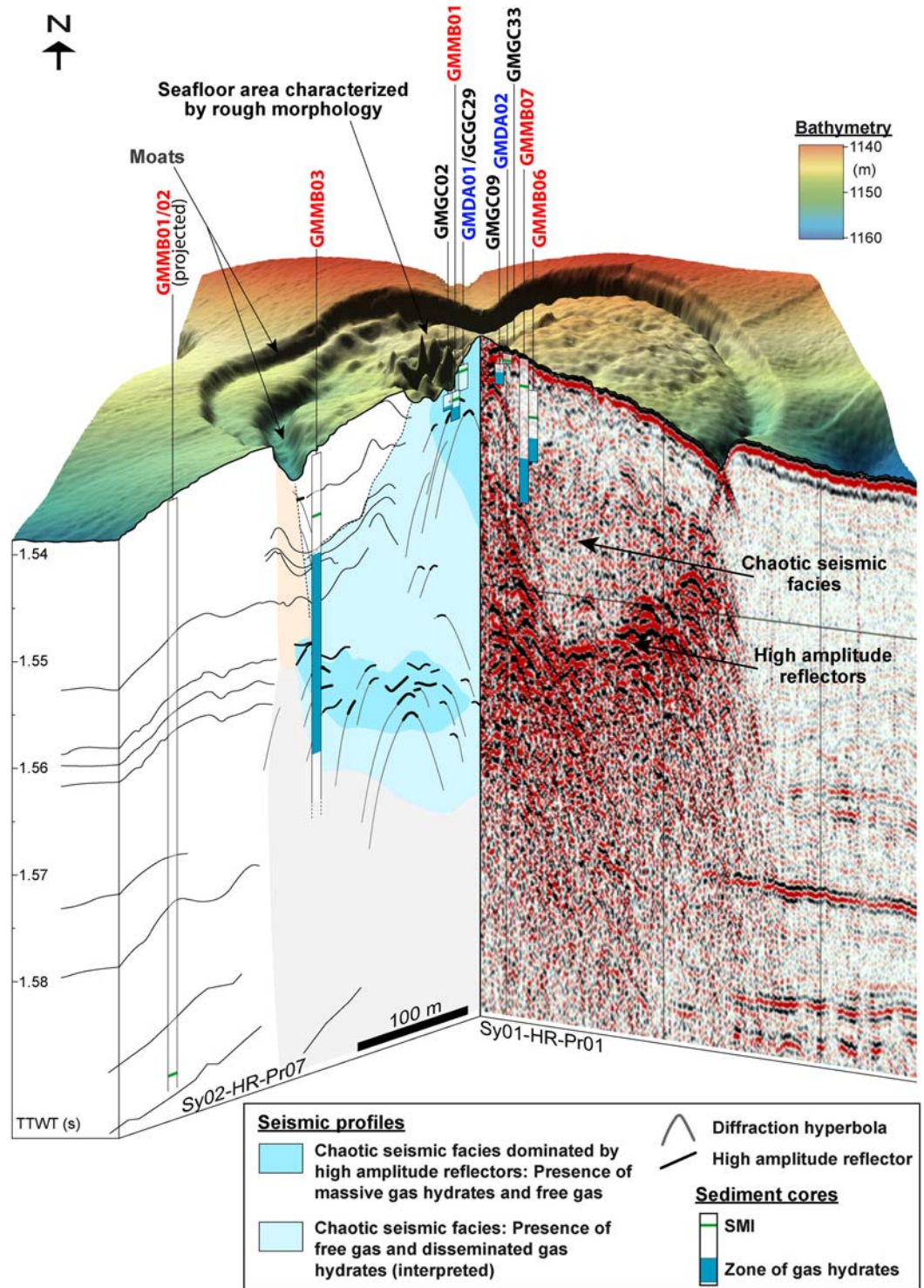
Figure 5. Three-dimensional interpretative view of Pockmark A comprising sea floor bathymetry, 2-D high-resolution seismic profile Sy01-HR-Pr01 (right; for location see Figure 1; taken from Sultan et al., 2010) and interpreted 2-D seismic profile Sy02-HR-Pr07 (left; modified after Sultan et al., 2010, 2014). Solid vertical lines indicate sea floor positions of selected cores (GMMB-: MeBo; GMGC-: gravity corer; GMDA-: Dynamic Autoclave Piston Corer) investigated in this study. Bars highlight subsurface positions of cores, depths of the SMI, and vertical distributions of gas hydrates. Shallowest SMI and ToGH indicate highest methane fluxes in the pockmark center. Existence of a clear SMI at about 1.595 s TTWT (~40 mbsf) at Site GMMB01/02 indicates methane fluxes sufficient to fuel AOM in areas distant to the sea floor depression.
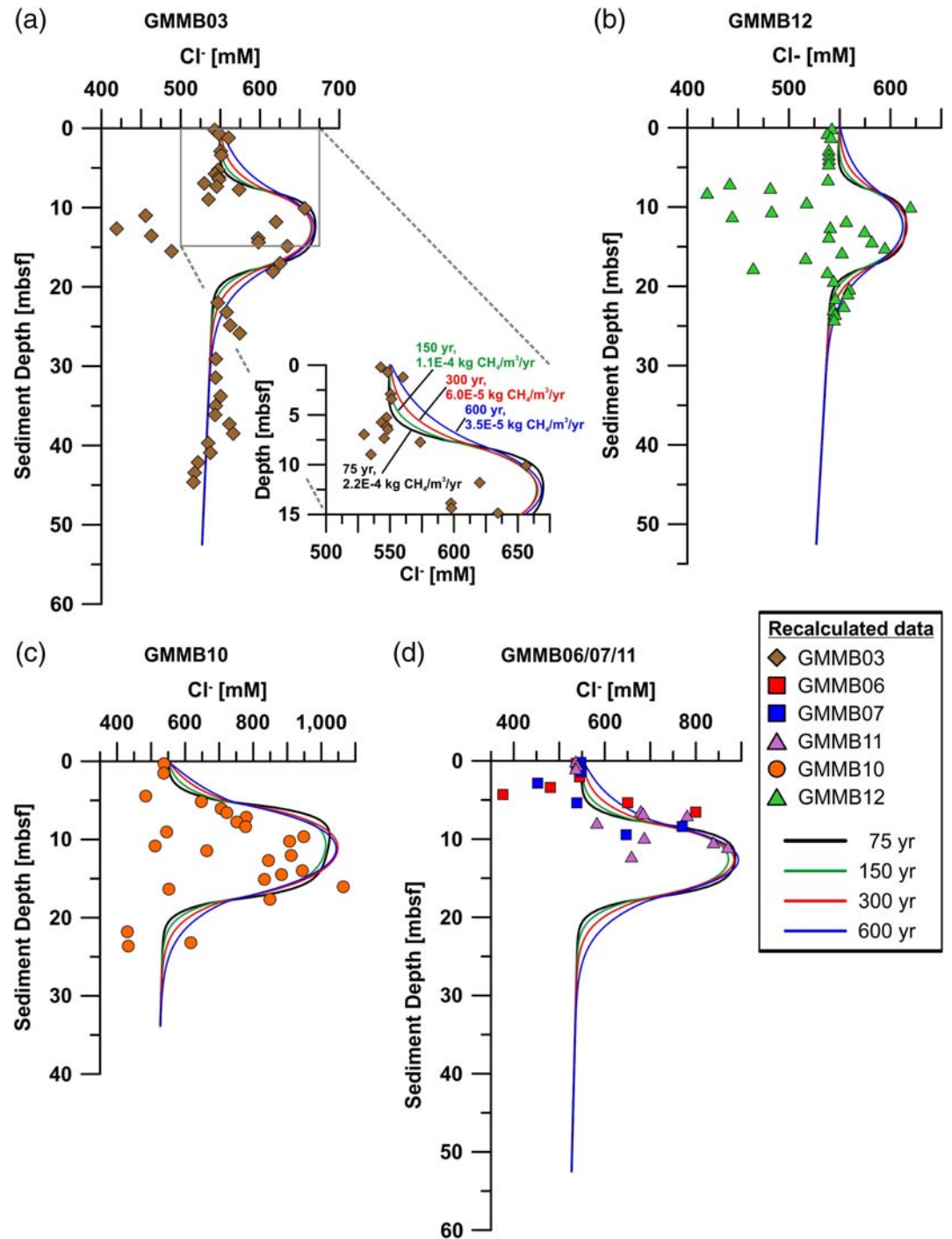
Figure 6. Modeled chloride concentration profiles at Sites (a) GMMB03, (b) GMMB12, (c) GMMB10, and (d) GMMB06/07/11. The model was run with different combinations of gas hydrate formation time and methane supply (as shown in the blowup of a). The longer time it takes to form gas hydrate, the weaker methane supply needed and therefore smoother chloride profile produced by the model. Therefore, only the longest time (and weakest methane supply) required can be constrained. The results show hydrate formation happened at most 300 years BP and most likely happened 75–150 years ago. Note: Chloride concentrations measured may be lower than in situ concentrations because of potential pore water dilution by hydrate-bound fresh water released during dissociation of hydrate pieces undetected in the sediment. Therefore, initial positive anomalies in chloride concentrations might have been higher than those measured, and times even shorter than those modeled. Chloride concentrations lower than those of sea water are also attributed to dilution from the chloride-depleted hydrate water released from dissociating hydrates during core recovery and handling (see, e.g., Hesse, 2003; Tréhu et al., 2004).

Table 3
Model-Derived Methane Input (in kg CH_4 (kg H_2O)$^{-1}$ year^{-1}) for the Different Time Scales Required to Induce Positive Chloride Concentration Anomalies Caused by Hydrate Formations at Selected MeBo Drill Sites

CH$_4$ input	GMMB03	GMMB12	GMMB10	GMMB 06/07/11	GMMB08
75 years	2.2E−4	1.4E−4	5.6E−4	4.4E−4	4.4E−4
150 years	1.1E−4	7E−5	2.8E−4	2.2E−4	2.2E−4
300 years	6E−5	4E−5	1.5E−4	1.2E−4	1.2E−4
600 years	3.5E−5	2.2E−5	8E−5	6.8E−5	6.8E−5

(~460 mM) relative to sea water. Positive chloride anomalies as high as 1,060 mM were detected at shallow sediment depth in particular for cores GMMB08, GMMB10, and GMMB11 from the central area characterized by rough sea floor morphology (Figure 3c). In addition, negative chloride excursions from background concentrations were detected from almost all central cores, and minimum concentrations of ~350 mM were found in GMDA03. Negative and positive chloride anomalies often occurred in adjacent samples with the negative chloride anomalies coinciding in most cases with soupy/moussy sediment textures.

4.4. Results From Numerical Modeling

4.4.1. Modeling of Concentration Profiles of Dissolved Chloride

Two free parameters, the strength of methane input and time needed for the modeled profiles to match the observations, control the distribution of pore water chloride in the model (see Table S2 for further information and Text S3 for boundary conditions used). Mathematically, these two free parameters cannot be solved with a single constraint (i.e., chloride enrichments) as the same chloride enrichment can be achieved in shorter time if a stronger methane source is assigned. An additional constraint comes from the shapes of the chloride profiles since they become smoother with increasing time as diffusion becomes more effective. Besides, if the supply of methane is too weak, diffusion can effectively transport the excess chloride toward the sea floor and result in leveling of chloride concentrations. For example, although the highest chloride enrichment observed by assigning the various combinations of methane flux and time (75 to 600 years; Figure 6a) can be reproduced, the chloride profiles produced from the two longer time scales (300 and 600 years) are too smooth compared to the observed profiles. In conclusion, our model is only able to constrain the minimum methane supply and longest time required to achieve the positive chloride anomalies observed. Moreover, results from the modeling of chloride concentration profiles may be considered as minimum estimates as freshening related to hydrate-dissociation during recovery could have caused dilution of in situ chloride concentrations.

By simulating different combinations of methane supply and time scale, as shown in Figure 6, it can be concluded that the chloride enrichment and, thus, the rapid hydrate formation must have occurred only very recently (within the last three centuries). For the sake of comparison, the time frame for hydrate formation at all sites was unified in order to derive relative methane inputs needed to explain the chloride enrichment observed (Table 3). We show that the strongest methane supply must have occurred in the subsurface below the "Rough Patch 1" (Sites GMMB10, GMMB06/07/11, and GMMB08), from which the gas-rich pressure cores (core codes "GMDA") were retrieved.

4.4.2. Modeling of Concentration Profiles of Dissolved Sulfate

For the sulfate modeling, we focused on three cores, GMMB01/02, GMMB03, and GMMB12 (Table 4), as for these cores sufficient data are available to reliably model their profiles. The last two cores were also used for the modeling of positive chloride anomalies that are indicative of recent hydrate formation (section 4.4.1). Sulfate was found over meter-scale depths within the sedimentary column for cores GMMB03 and GMMB12 (Figures 3b and 7). The sulfate profiles are characterized by two segments with an upper segment (0 to ~300 cmbsf) showing concentrations close to sea water and a narrow deeper segment, which shows a sharp decline in concentrations close to zero (~300–360/525 cmbsf, respectively). The abrupt change in the sulfate gradient suggests a non-steady-state system, where the initial conditions correspond to vertical profiles resulting from penetration of sea water-derived sulfate over the entire length domain.

In the case of joint cores GMMB01/02 outside the pockmark, a smooth and linear decrease in sulfate concentrations with depth is observed over the top 30 mbsf followed by a sharp decrease to concentrations close to zero at the SMI at around 40 msbf. The model used herein considers a methane pulse followed by rapid

Table 4
Model Results for the Sulfate-Profiles Evolution With Time

Core code	Top of the hydrate layer (mbsf)	Time elapsed to reach present-day profile (year)
GMMB01/02	42[a]	$18,700 \pm 2,500$
GMMB03	6.9	75 ± 15
GMMB12	7.5	100 ± 15

[a]For GMMB01/02, the top of the gas hydrate (ToGH) layer was extrapolated considering an average distance between the SMI and the ToGH of approximately 2 m. Depth of the SMI at GMMB01/02 at 40 mbsf according to Sultan et al. (2014) and Wei et al. (2015).

hydrate formation that settled the methane source as being the ToGH at around 40 mbsf, and we simulated the evolution of the sulfate profile over time.

5. Discussion

5.1. Origin of Hydrocarbons, Hydrate Distributions, and Quantities
5.1.1. Origin of Hydrocarbons

In this study, genetic diagrams recently proposed for source assignments of light hydrocarbons (Milkov & Etiope, 2018) were considered. In the diagram C_1/C_{2+} versus $\delta^{13}C$-CH_4 all samples of hydrate-bound hydrocarbons plot close to the boundary between the fields assigned for primary microbial light hydrocarbons and secondary microbial hydrocarbons (Figure 4a). Those molecular and isotopic compositions may be explained by upward migration of secondary microbial methane and/or late mature thermogenic hydrocarbons and admixture with primary microbial methane in shallow sediments. Thermogenic hydrocarbons and secondary microbial hydrocarbons are commonly attributed to degradation of kerogen and petroleum, respectively (Milkov, 2011; Tissot & Welte, 1984).

In the diagram $\delta^{13}C$-CH_4 versus δ^2H-CH_4 hydrate-bound hydrocarbons also plot within the overlapping fields assigned for secondary microbial and late mature thermogenic hydrocarbons (Figure 4b). However, in contrast to hydrocarbon source interpretations deduced from Figure 4a, Figure 4b suggests an additional contribution from oil-associated biodegraded thermogenic hydrocarbons. In conclusion, from relationships between molecular hydrocarbon ratios, $\delta^{13}C$-CH_4, and δ^2H-CH_4, hydrocarbons from various sources comprising late mature thermogenic, primary microbial (from carbonate reduction), secondary microbial (from petroleum biodegradation), and oil-associated hydrocarbons seem to prevail at Pockmark A. A similar mixture of deep thermogenic hydrocarbons and admixtures of shallow microbial hydrocarbons is also assumed for the nearby pockmark cluster C (de Prunelé et al., 2017; Figures 1b and 1c). However, $\delta^{13}C$ values of ethane (-34%) and carbon dioxide (-3%) of those samples (de Prunelé et al., 2017) as well as their carbon isotope separations (($\Delta\delta^{13}C(CH_4–C_2H_6) = 16.5\%$; $\Delta\delta^{13}C(CH_4–CO_2) = 47.5\%$) do not indicate severe hydrocarbon biodegradation (see, e.g., Milkov, 2011).

The observed relative methane enrichment in shallow gas hydrates that results in comparably high C_1/C_{2+} ratios may also be explained by adsorption of wet gas components on clay minerals or organic matrices (Prinzhofer & Pernaton, 1997), differential molecular diffusion during migration (Milkov & Etiope, 2018; Schoell, 1983), and/or gas hydrate formation. However, different diffusion behaviors of individual light hydrocarbons as possible cause of the relative depletion in C_+ hydrocarbons might be excluded since ebullition of gas is believed to be the major transport mechanisms for fluids ascending toward the sea floor at the pockmark (Sultan et al., 2014). Furthermore, evidence for the presence of deeply buried sII or sH hydrates that may entrap C_{2+} hydrocarbons at depth causing relative methane enrichment in the upward migrating gas (e.g., Paganoni et al., 2016) has not been observed neither during MeBo drilling as part of this study nor from previous seismic surveys. In contrast, preferential enrichment in methane during crystallization of sI hydrate (e.g., Pape et al., 2010, and references cited therein) in the shallow pockmark sediment and concurrent exclusion of C_{3+} hydrocarbons from the hydrate may have contributed to the molecular composition of hydrate-bound hydrocarbons.

Relatively uniform stable carbon isotopic compositions of methane in all samples of hydrate-bound gas analyzed ($n = 21$) suggest that the pockmark-associated hydrates are fueled from similar hydrocarbon sources independent from their distance to the pockmark center. However, slightly more negative $\delta^{13}C$ signatures measured for methane in shallow hydrates retrieved with the gravity corer compared to those in deeper (>7.4 mbsf) hydrates collected with MeBo substantiate additional incorporation of microbial methane relatively depleted in ^{13}C. A shallow production of microbial hydrocarbons was already proposed for ^{13}C depletions in methane ($\delta^{13}C$-$CH_4 \leq -86\%$) at depth of the SMI in sediments recovered from Pockmark C2 located about 2.3 km SSE of Pockmark A (de Prunelé et al., 2017; see Figures 1b and 1c for position).
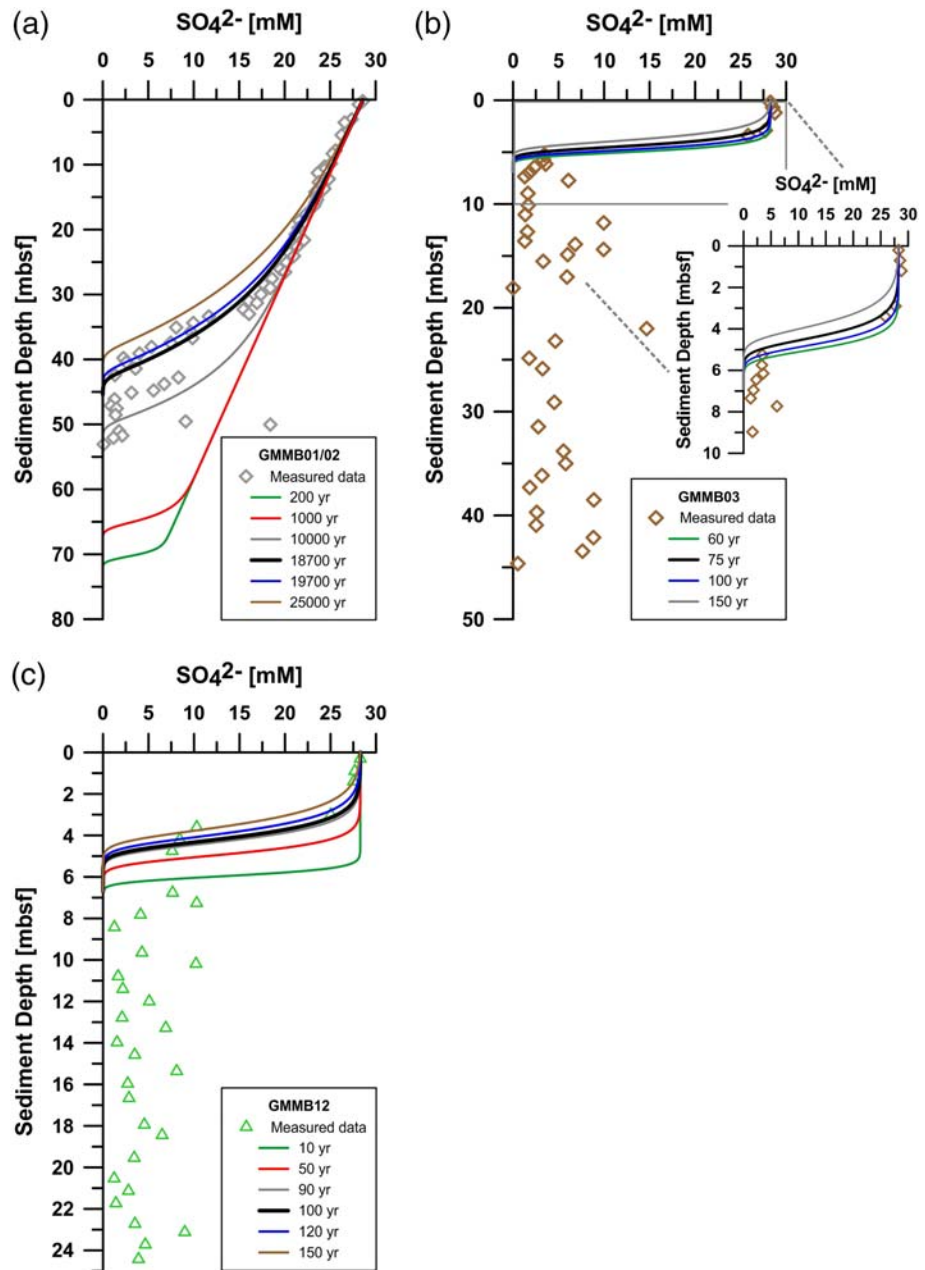
Figure 7. Modeled evolution of the sulfate concentration profiles (measured concentrations) over time at Sites GMMB01/02, GMMB03, and GMMB12. The model assumes that the sulfate profile starts evolving from the establishment of the hydrate layer. The results indicate that the hydrate layers supplying methane for AOM formed between around 60 and 150 years ago at Sites GMMB03 and GMMB12 with best fit obtained for ages between 75 and 100 years. At Site GMMB01/02 outside the sea floor depression a best fit for the extrapolated ToGH was obtained for ages of 18.7 ± 1 kyr.

Formation temperatures of thermogenic methane are believed to range from 70°C to 250°C with a peak at around 150°C (Hunt, 1996; Quigley & Mackenzie, 1988). Assuming that geothermal gradients measured inside Pockmark A (locally up to 258°C km^{-1}; Wei et al., 2015) and outside the pockmark (72°C km^{-1}; Wei et al., 2015) follow a linear trend with depth, overall formation depths calculated for thermogenic hydrocarbons range between ~0.3 and 3.5 km. For the fraction of late mature thermogenic hydrocarbons that likely prevails thermogenic hydrocarbons at Pockmark A (Figure 4b), formation temperatures exceeding 150°C (Hunt, 1996) and formation depths ranging between 0.6 km (258°C km^{-1}) and 2.1 km

($72°C$ km^{-1}), respectively, are assumed. Such estimated formation depths correspond to the presence of an intermediate hydrocarbon reservoir between 500 and 580 mbsf below the nearby pockmark cluster C ("hydrocarbon storage zone" in de Prunelé et al., 2017). This suggests that major formation of late mature thermogenic hydrocarbons in this area takes place below the depth of the hydrocarbon storage body.

Petroleum biodegradation resulting in the formation of secondary microbial methane, which is believed to also occur at Pockmark A, was reported to mostly occur at temperatures below 80°C (Milkov, 2011; Wilhelms et al., 2001). Oil was found in the study area impregnating shallow sediments in the nearby Pockmark B (de Prunelé et al., 2017; Figures 1b and 1c). Consequently, secondary microbial methane formation is expected to take place within the uppermost ~1 km of the sedimentary column. The temperature range tolerated by methanogenic archaea that form primary microbial hydrocarbons is also limited to temperatures below ~80°C (Valentine, 2011) and, thus, restricted to the upper 1 km.

5.1.2. Distributions and Quantities of Gas Hydrate and Methane

The presence of gas hydrates in shallow sediments of Pockmark A was proposed to result from gas supply trough fracture systems connected to the "intermediate gas reservoir" (Sultan et al., 2014; Taleb et al., 2020) (Figure 1d). This assumption is corroborated by the fact that natural (Figure 1d) and drilling-induced sea floor gas emissions (GMMB10/11; Figure 1e) have been observed to be spatially related to the central major fracture, suggesting that highly focused free gas migration occurs through the fracture system. The presence of very shallow (<1 mbsf) gas hydrates indicates methane concentrations exceeding solubility in shallow sediments in both, "Rough Patch 1" and "Rough Patch 2" (Table 1) in 2011 and support this assumption. Distributions of soupy/moussy sediment textures observed in MeBo cores indicated that the lower limit of the hydrate-charged sediment body was located at about 25 mbsf (Table S1). This depth assignment is supported by results from seismic profiling (Sultan et al., 2014), thermal imaging and pore water chlorinity investigations (Wei et al., 2015), as well as geotechnical sounding (Taleb et al., 2018).

However, variable depths of both, the SMI and the ToGH, on a small horizontal scale substantiate considerable heterogeneity in methane and hydrate distribution within the upper sediment column (Figures 1c and 5; Tables 1 and 2). For instance, a comparably shallow SMI (0.3 mbsf) and maximum $GHsat_{tr}$ (51.2% pv) were detected in pressure core GMDA03 from "Rough Patch 1". In contrast, a deeper SMI (1.25 mbsf in GMDA05) and the absence of gas hydrates indicated by relatively low gas quantities and uniform chloride concentrations was observed in cores GMDA05 and GMDA06. These two cores were located approximately 18 m northeast of GMDA03 at the northern rim of "Rough Patch 1" (Figures 1 and 2; Table S1).

Pressure cores taken from the rough patches of Pockmark A in 2011 revealed unusually high hydrate concentrations at specific sites. DAPC core GMDA03 recovered from "Rough Patch 1" contained the highest $GHsat_{tr}$ (51.2% pv) of all DAPC cores taken at cold seeps (Heeschen et al., 2007; Pape et al., 2011a) and mud volcanoes (Pape et al., 2011b) in other regions, so far. However, considering the strongly heterogeneous spatial distribution of hydrates and variable hydrate saturations (Table 2), we refrain from estimating total amounts of methane bound in shallow hydrates at Pockmark A and state that 3.2% pv (core GMDA01, "Rough Patch 1") is a minimum hydrate saturation. Nevertheless, the hydrate saturations obtained from pressure coring in this study substantiate that shallow hydrates in deepwater pockmarks have a significant methane storage capacity. In this context, it is worth mentioning that continuous intervals of deeper (greater than ~33 mbsf) massive gas hydrates several meters in lengths have been collected by drilling at the margins of a large pockmark located at the Umitaka Spur in the Japan Sea (Snyder et al., 2020).

Order-of-magnitude estimates of dissolved methane concentrations in hydrate-free sediments below the sulfate zone can be obtained by considering data from pressure core GMDA05. Provided that the 4.82 L of gas (99 vol.% CH_4: 0.21 mol CH_4) exclusively originated from pore water exsolution from the 119 cm-long interval (approximately 6.84 L bulk sediment volume, average porosity of 83%: 5.68 L pore volume) in between the base of the sulfate zone (1.25 mbsf) and the core bottom (2.44 mbsf), this would result in an estimated average concentration of dissolved methane of approximately 0.04 mol CH_4 dm^{-3} pore volume.

Elevated concentrations of dissolved methane found below the hydrate-charged sediment body beneath "Rough Patch 1" (GMMB08), close to the pockmark rim (GMMB03), and even outside of the pockmark (GMMB01/02) (Figure 3a) demonstrate that methane is not only transported through the central fracture system. Relative methane enrichments in deeper pockmark sediments may be explained by lateral fluid flow below the hydrate-charged body caused by clogging of the fracture system through hydrate accumulations

(see, e.g., Römer et al., 2012; Sultan et al., 2014). Reduction of sediment permeability due to a decrease of porosity in the course of hydrate saturation in overlying sediments (e.g., Daigle & Dugan, 2011; Flemings et al., 2003; Nimblett & Ruppel, 2003) may add to this process. For Site GMMB01/02, Sultan et al. (2016) have additionally proposed that coarse-grained sediment intervals located at depths beneath the sediments studied herein (>32 mbsf) have served as potential horizontal transport pathways during phases of high gas pressure in the "intermediate gas reservoir." Free gas accumulations below the hydrate zone as imaged in Figure 5 may also be fueled by fluid migration along secondary fractures that have been illustrated by Sultan et al. (2010), and/or methane upward diffusion. Diffusion of deep-sourced thermogenic hydrocarbons into shallow sediments at a site about 5 km apart from an actively gas-emitting pockmark has been shown (Pape et al., 2020).

5.2. Modeling Results—Formation of Gas Hydrates and Evolution of the SMI

5.2.1. Chloride Concentration Anomalies as an Indicator of Recent Gas Hydrate Formation Stimulated by Supply of Free Methane Gas

Strong enrichments in dissolved chloride up to 1,060 mM in cores GMMB06, GMMB07, GMMB08, GMMB10, and GMMB11 indicate that the abundant gas hydrate is a result of rapid gas hydrate formation in the pockmark center. Such rapid hydrate formation may be related to additional methane input from a free gas phase (Haeckel et al., 2004; Peszynska et al., 2016; Torres et al., 2004, 2011). Indeed, putative fractures that may serve as pathways for rapid gas migration were penetrated during drilling of GMMB10 at about 24 mbsf and GMMB11 at 12.5 mbsf triggering temporary discharge of substantial volumes of gas from the sea floor (Sultan et al., 2014). In addition, the presence of porous hydrate specimen indicated the occurrence of bubble-forming gas under water-limited conditions in the immediate subsurface at the center.

Gas hydrate distribution in Pockmark A is highly heterogeneous (section 5.1.2; Wei et al., 2015), and a systematic trend in gas hydrate saturations among the drill sites is therefore not expected. Nevertheless, an agreement in GHsat derived from pressure core degassing (GHsat$_{tr}$) and chloride modeling (GHsat$_{mod}$) is observed from cores retrieved from similar locations (Tables 1 and 2). For instance, the highest GHsat$_{tr}$ was measured from pressure core GMDA03 (51.2% pv; 0.30–0.77 mbsf) in "Rough Patch 1", which was located ~35 m NW of MeBo core GMMB10. This MeBo core showed one of the highest chloride concentrations measured in the study area (1,065 mM at 9.64 cmbsf), yielding GHsat$_{mod}$ of 46% pv. Admittedly, the coherent values of GHsat$_{tr}$ and GHsat$_{mod}$ from three pairs of comparisons (see Table 2) can be coincidence. Nonetheless, the similar magnitude in GHsat suggests that our model provided reasonable estimations of gas hydrate abundances. As the GHsat$_{mod}$ is mainly a function of the strength of methane supply assigned, a tight link between methane supply and gas hydrate abundance in this pockmark is expected.

In addition to the similarity analysis of GHsat$_{tr}$ and GHsat$_{mod}$, time scales estimated from the chloride model can be verified against the results from pressure cores. By dividing the amount of methane recovered in pressure cores with the rate of methane supply estimated from the chloride model (Table S5), a time scale can also be calculated. Calculations were performed on three pairs of MeBo and pressure cores that are in close vicinity to each other: GMMB06/07/11 versus GMDA02, GMMB10 versus GMDA03, and GMMB12 versus GMDA04. At Site GMDA02 a time scale of 33–66 years is estimated. Longer time scales of 86–171 and 171–342 years were calculated from GMDA03 and GMDA04, respectively. These calculations are remarkably similar to estimations from chloride modeling (<300 years) and, thus, substantiate the very recent and dynamic gas hydrate formation in Pockmark A. Moreover, the calculations derived in this study are in line with the calculated time (80–130 years) that has elapsed since an assumed lateral migration of methane-rich fluid below 32 mbsf at Site GMMB01/02 (Sultan et al., 2016). These results confirm that rapid hydrate accumulation controlled the formation and evolution of Pockmark A as suggested by Sultan et al. (2014) and provide a time constraint (less than three centuries) for this process. Supportive results come from an independent study at three pockmarks located a few kilometers south to Pockmark A (pockmark cluster C; de Prunelé et al., 2017), where hydrate formation ages with similar orders of magnitudes were obtained.

5.2.2. Methane Fluxes Inferred From Sulfate Profiles

Episodic methane fluxes from below Pockmark A in the past were inferred from abundant authigenic high Mg-calcite and aragonite co-occurring in surface sediments (Fontanier et al., 2014). This assumption is in

line with a proposed scenario of fast hydrate formation within the pockmark caused by cycles of accumulation of free gas accompanied with pressure increase within the clay-rich sediment followed by the formation/reopening of fractures that enables gas release from the reservoir and upward migration (Sultan et al., 2014). The newly formed hydrate layers serve as methane source for the AOM reaction in overlying sediments. This idea is supported by the short distance between the ToGH and the SMI in the cores investigated (Table 1). Thus, by considering this conceptual scheme and modeling the evolution of the sulfate profiles over time since the methane injection, we estimated the age of the hydrate layers at Sites GMMB01/02, GMMB03, and GMMB12 (Table 4; Figure 7). Such simulations revealed that the upper hydrate layers within the depression have been formed around 75 years ago at Site GMMB03 and 100 years ago at Site GMMB12, respectively. Outside the pockmark, at Site GMMB01/02, an age of around 18,700 years was calculated for the extrapolated ToGH. The sulfate profile-derived ages of the hydrate layers obtained for the cores located within Pockmark A match the estimates obtained for the development of the positive chloride anomalies caused by hydrate formation (see section 5.2.1). It is worth mentioning that, although gas advection and pore water advection may be decoupled (Hong et al., 2018), both models independently applied in this study revealed relatively weak pore water advection in general ($\sim 1.7 \times 10^{-4}$ m year^{-1}; Figures S4). Ages of hydrate layers calculated for Pockmark A also correspond to ages of hydrate layers within the nearby Pockmarks C1 (80 ± 10 years) and C3 (21 ± 2 years) as obtained from sulfate profile modeling of single sediment cores (de Prunelé et al., 2017; Figure 1b). These agreements suggest that trends in the sulfate profiles are most likely related to hydrate dynamics rather than other processes known to cause similar shapes in profiles (see, e.g., Fischer et al., 2013; Hensen et al., 2003). Remarkably, U/Th dating of carbonate breccia demonstrated that Pockmark C3 has additionally been very active within the period 13–2.5 kyr BP (Bayon et al., 2015). During that period, methane pulses have triggered accumulation of shallow hydrates that subsequently underwent decomposition. Anaerobic oxidation of the methane released fueled aragonite precipitation above the ToGH. The processes of hydrate formation and decomposition have caused severe fluctuations of the SMI depth.

The abrupt change in the pore water sulfate gradient at Site GMMB01/02 (Figures 4b and 7) indicates methane injection rather than constant diffusion. Moreover, the age of the hydrate layer supplying the AOM demonstrates that Pockmark A has been active since the phase of sea level and temperature rise subsequent to the Last Glacial Maximum (LGM) at least (e.g., Fleming et al., 1998; Rohling et al., 1998) extending the previous estimate of 13 kyr determined for Pockmark C3 (Bayon et al., 2015). Remarkably, similar minimum ages of pockmark activity (ca. 21 kyr) were also obtained by dating of carbonates associated to hydrate-bearing pockmarks at about 670 m water depth, up slope of the Niger Delta (Ruffine et al., 2013).

In general, a continuous increase of approximately 10% in hydrostatic pressure caused by sea level rise subsequent to the LGM as estimated for our study site would have promoted hydrate stability. However, Bangs et al. (2005) proposed an upward shift of the BGHSZ and release of free gas into sediments below following postglacial bottom sea water warming and shift of the geothermal gradient in Hydrate Ridge, offshore Oregon. In case such free gas happens to migrate upward through fracture systems, it may lead to precipitation of gas hydrates in shallow sediments (e.g., Daigle et al., 2011; Tryon et al., 1999). However, a tight link between such processes and the formation of the hydrate layers investigated at Pockmark A is unlikely. The oldest hydrate layer was formed during the LGM when bottom water temperatures were lower than today. In contrast, the youngest layers precipitated within the past two centuries when the increase in hydrostatic pressure compared to LGM conditions had stabilized and promoted hydrate stability already. In addition, an expected postglacial deep water warming by less than 4°C (Waelbroeck et al., 2002) was insufficient to cause gas release induced by gas hydrate dissociation in shallow sediments of Pockmark A (see also section 5.3 and Figure S4). Therefore, methane injections and gas hydrate formations are likely not directly triggered by climate-driven changes in sea level and bottom sea water temperature. In contrast, internal dynamics of the subsurface petroleum and fluid flow system appear to be likely causes of the methane pulses in Pockmark A.

5.3. Shallow Gas Hydrates Affecting Pockmark Morphology

In Pockmark A, two seabed types can be differentiated with respect to gas and gas hydrate contents and morphology. The area around the rough patches is characterized by relatively smooth surfaces (Figure 1d), low methane concentrations in the shallow sediments as indicated by the low sea floor backscatter in 2004

(George & Cauquil, 2007; Figure 2) and a comparably deep ToGH at ≥6.9 mbsf in 2011 (Table 1). In contrast, the two central rough patches show a generally negative relief, a high-backscatter reflectivity, and host considerable amounts of shallow gas hydrates (Tables 1 and 2; Figure 2). Such properties of the two seabed types in Pockmark A match those of the diffuse and the focused fluid flow regimes reported for the Regab pockmark at the Congo deep sea channel (Marcon et al., 2014). At Pockmark A, a free methane gas phase was present in the shallow subsurface of the rough patches in 2011, as evidenced by the sea floor gas emissions near the major fracture and the recovery of porous hydrate specimen. Pronounced loss of sediment from the rough patches is indicated by their basic negative relief.

A chaotic sea floor morphology at gas-charged sites within the GHSZ was previously explained by (i) sediment resuspension by upward gas flow (e.g., Kannberg et al., 2013; O'Regan et al., 2015; Panieri et al., 2017; Sahling et al., 2008), (ii) sediment up-doming due to gas overpressure (e.g., Koch et al., 2015; Zander et al., 2020) or hydrate growth (potentially followed by collapse during hydrate dissolution; e.g., Riboulot et al., 2016; Römer et al., 2012; Serié et al., 2012; Sultan et al., 2010), and (iii) detachment of hydrate chunks from the sea floor (e.g., Charlou et al., 2004; Kannberg et al., 2013; MacDonald et al., 1994; Pape et al., 2011a; Paull et al., 1995; Suess et al., 2001). For pockmarks at Vestnesa Ridge, Arctic Ocean, Panieri et al. (2017) demonstrated that subvertical gas chimneys in the subsurface terminated into pit-like sea floor depressions from which gas emissions into the water column were fueled. Because the natural gas emissions at Pockmark A originated from a site within or close to pits in "Rough Patch 1", it is plausible to assume that formation of the pits resulted from localized gas bubble discharge as well.

The sea floor gas emission site fueling the only two gas bubble plumes recognized in 2011 in the water column above Pockmark A were likely linked to shallow fractures (Sultan et al., 2014) and, thus, restricted in spatial dimensions. In contrast, the two rough patches jointly covered ~11% of the area of Pockmark A. Therefore, the presence of several partly coalescing pits, as particularly observed in "Rough Patch 1", may be explained by deflection of migration pathways due to clogging of fracture systems by hydrates (Bangs et al., 2011; Liu & Flemings, 2007; Simonetti et al., 2013). In addition, the present-day appearance of Pockmark A most likely results from several fluid migration events involving multiple pathways. The extent of lateral migration of gas discharge sites at the sea floor in the past is unknown. However, the sizes of the rough patches and their spatial association with dense occurrences of shallow hydrates suggest that additional, hydrate-related processes have contributed to the formation of local sea floor depressions and rough sea floor morphologies.

Formation and decomposition of shallow gas hydrates alone are insufficient to explain the sea bed morphology. In 2011, a prevalence of hydrate formation over destabilization was indicated by the positive anomalies in chloride concentrations. Hydrate formation is associated with volume expansion since the specific density of massive gas hydrates (~0.91 g cm^{-3}) is lower than that of pore water (~1.03 g cm^{-3}). However, extensive sediment doming due to gas overpressure or hydrate formation is not supported by the negative morphology in the rough patches. Nevertheless, sediment doming followed by erosion of exposed sea floor in the past cannot be ruled out.

Moreover, variations in fluid and bottom water temperatures likely do not directly affect sea bed morphology. For other gas hydrate sites, focused upward flow of warm fluids resulting in hydrate dissociation and an increase in gas pressure below the BGHSZ has been proposed (e.g., Römer et al., 2012; Wood et al., 2002). Numerical simulations have shown that temperature increases by several degrees above background values in chimney-like migration pathways (Liu et al., 2019) and in shallow sediments (Zander et al., 2020) can result from ongoing gas hydrate formation. However, at Pockmark A sI hydrates are stable in an ~35 m-thick GHSZ even at the maximum geothermal gradient of 258°C km^{-1} measured in 2011 (Wei et al., 2015). In addition, results of temperature modeling conducted in this study (section S3.2) suggest that an increase of bottom sea water temperature by about 10°C would be required to force dissociation of gas hydrates in the topmost two meters of sediment.

In contrast, sporadic sea floor hydrate detachment is proposed to have contributed to the negative relief and the rugged sea floor. Density calculations performed in this study have shown that a fraction of ≥20 vol% of porous gas hydrate in a unit cell of sediment would result in a bulk (porous gas hydrate + wet sediment) density that is lower than that of bottom sea water (see Text S5). Nominal pore space occupations exceeding these threshold values were recorded by means of pressure cores GMDA02, GMDA03, and GMDA04,

demonstrating that rafting of porous hydrates is a realistic mechanism contributing to the rugged sea floor morphology. Furthermore, the presence of free gas within the GHSZ as observed at Sites GMMB10 and GMMB11 and on seismic records (Figure 5; Taleb et al., 2020) may facilitate detachment of sediments hosting even lower proportions of porous hydrates.

This process may also be supported by the dynamic behavior of deeper gas hydrates on variations in the geothermal gradient. The spatially very heterogeneous temperature gradients (72°C km^{-1} to 258°C km^{-1}; Wei et al., 2015) are likely also associated with temporal variations. Even though only gas hydrates below the shallowest BGHSZ at ~35 mbsf will be affected, a strong change of geothermal gradients near gas expulsion from faults as well as possible shifting of gas expulsion sites may cause gas hydrate layers to form and decompose quickly. Uptake or addition of free gas leading to drop or built-up of pressure will promote rafting of residual gas hydrates.

In summary, the features observed at Pockmark A match with previously proposed models with localized sea floor gas discharge causing sediment resuspension and formation of pits, temporary sealing of vent sites by hydrate formation, reopening of migration pathways due to gas accumulation and pressure build-up, pulses of sea floor gas expulsion, and further sea floor disturbance by hydrate rafting.

6. Conclusions

This study describes for the first time the interrelationship between actual quantities and distributions of gas hydrates, the chronology of fluid migration events, and major factors shaping the sea floor at a deep sea pockmark. Pockmark A situated in a deepwater region offshore Nigeria that comprises significant hydrocarbon reservoirs was analyzed during a collaboration between the French IFREMER and the German MARUM in 2011 with different methods in order to (i) determine hydrate quantities and distributions, (ii) assess the timing of fluid migration and gas hydrate formation, and (iii) evaluate hydrate-related processes affecting the sea floor morphology. The pockmark forms a subcircular sea floor depression ~500–600 m in diameter and was classified as active with regard to gas injection into shallow sediments in the recent past and the presence of young gas hydrates as attested by pronounced positive anomalies in pore water chloride concentrations.

Shallow pressure coring at six sites with the Dynamic Autoclave Piston Corer revealed integral gas hydrate saturations reaching up to 51.2% of pore volume near a fracture system crossing the pockmark center. The maximum hydrate saturations observed for the shallow sediments of Pockmark A are the highest hydrate saturations in all hydrocarbon-rich settings examined by this technique, so far. However, hydrate distributions showed a high lateral and vertical variability. Molecular hydrocarbon compositions and methane stable isotope signatures in combination with geothermal gradients known from previous studies at Pockmark A suggest that shallow hydrates are predominantly fueled by late mature thermogenic hydrocarbons likely formed at depths exceeding 1.6 km below sea floor that are mixed with secondary microbial methane from petroleum degradation and primary microbial hydrocarbons during upward migration.

Two independent modeling approaches using pore water sulfate and chloride distributions in the up to 56.7 m-long sediment cores drilled with the robotic sea floor drill rig MARUM-MeBo70 were successfully applied to assess the time elapsed since the last major methane input leading to hydrate formation. Model results from positive chloride concentration anomalies in pore waters suggest that the last major phase of chloride enrichments in the course of hydrate precipitation occurred during the past three centuries with best fits between 75 and 150 years before present. Results from modeling of present-day sulfate profiles also demonstrated that hydrate layers formed within the last century, in agreement with the chlorinity modeling. Highest methane input rates were obtained for MeBo cores taken from the pockmark center where uppermost sediments are characterized by high backscatter and a rough sea floor topography.

Two areas in the central part of the pockmark characterized by sea floor depressions with rugged morphology indicate recent activity of the fluid system. Pits at the sea bed in these areas most likely result from sediment resuspension and removal associated to episodic, localized gas bubble discharge. Detachment of sediment piles hosting porous hydrates and free gas supported by pressure build-up of free gas beneath probably have contributed to the rough sea floor.

Data Availability Statement

Data used in the present paper are covered by a confidentiality agreement between TOTAL, IFREMER, and MARUM that restricts access. Geochemical data and specifics of MeBo cores are made available through the World Data Center PANGAEA® (http://www.pangaea.de, Pape & Bohrmann, 2020). Additional information is available to interested readers on request.

References

Abegg, F., Hohnberg, H. J., Pape, T., Bohrmann, G., & Freitag, J. (2008). Development and application of pressure-core-sampling systems for the investigation of gas- and gas-hydrate-bearing sediments. *Deep-Sea Research I: Oceanographic Research Papers*, *55*(11), 1590–1599. https://doi.org/10.1016/j.dsr.2008.06.006

Bangs, N. L. B., Hornbach, M. J., & Berndt, C. (2011). The mechanics of intermittent methane venting at South Hydrate Ridge inferred from 4D seismic surveying. *Earth and Planetary Science Letters*, *310*(1–2), 105–112. https://doi.org/10.1016/j.epsl.2011.06.022

Bangs, N. L. B., Musgrave, R. J., & Tréhu, A. M. (2005). Upward shifts in the southern Hydrate Ridge gas hydrate stability zone following postglacial warming, offshore Oregon. *Journal of Geophysical Research*, *110*, B03102. https://doi.org/10.1029/2004JB003293

Bayon, G., Henderson, G. M., Etoubleau, J., Caprais, J.-C., Ruffine, L., Marsset, T., et al. (2015). U-Th isotope constraints on gas hydrate and pockmark dynamics at the Niger delta margin. *Marine Geology*, *370*, 87–98. https://doi.org/10.1016/j.margeo.2015.10.012

Bayon, G., Pierre, C., Etoubleau, J., Voisset, M., Cauquil, E., Marsset, T., et al. (2007). Sr/Ca and Mg/Ca ratios in Niger Delta sediments: Implications for authigenic carbonate genesis in cold seep environments. *Marine Geology*, *241*(1–4), 93–109. https://doi.org/10.1016/j.margeo.2007.03.007

Berner, R. A. (1980). *Early diagenesis: A theoretical approach (pp. 256)*. Princeton: Princeton University Press. https://doi.org/10.1515/9780691209401

Bhatnagar, G., Chapman, W. G., Dickens, G. R., Dugan, B., & Hirasaki, G. J. (2008). Sulfate-methane transition as a proxy for average methane hydrate saturation in marine sediments. *Geophysical Research Letters*, *35*, L03611. https://doi.org/10.1029/2007GL032500

Boetius, A., Ravenschlag, K., Schubert, C. J., Rickert, D., Widdel, F., Gieseke, A., et al. (2000). A marine microbial consortium apparently mediating anaerobic oxidation of methane. *Nature*, *407*(6804), 623–626. https://doi.org/10.1038/35036722

Bohrmann, G., Greinert, J., Suess, E., & Torres, M. (1998). Authigenic carbonates from the Cascadia subduction zone and their relation to gas hydrate stability. *Geology*, *26*(7), 647–650. https://doi.org/10.1130/0091-7613(1998)026<0647:ACFTCS>2.3.CO;2

Borowski, W. S., Paull, C. K., & Ussler, W. III (1996). Marine pore-water sulfate profiles indicate in situ methane flux from underlying gas hydrate. *Geology*, *24*(7), 655–658. https://doi.org/10.1130/0091-7613(1996)024<0655:MPWSPI>2.3.CO;2

Boudreau, B. P. (1997). *Diagenetic models and their implementation: Modelling transport and reactions in aquatic sediments (pp. 436)*. Berlin: Springer-Verlag. https://doi.org/10.1007/978-3-642-60421-8

Brooks, J. M., Bryant, W. R., Bernard, B. B., & Cameron, N. R. (2000). The nature of gas hydrates on the Nigerian continental slope. *Annals-New York Academy of Sciences*, *912*(1), 76–93. https://doi.org/10.1111/j.1749-6632.2000.tb06761.x

Bünz, S., Polyanov, S., Vadakkepuliyambatta, S., Consolaro, C., & Mienert, J. (2012). Active gas venting through hydrate-bearing sediments on the Vestnesa Ridge, offshore W-Svalbard. *Marine Geology*, *332–334*, 189–197. https://doi.org/10.1016/j.margeo.2012.09.012

Carson, B., Seke, E., Paskevich, V., & Holmes, M. L. (1994). Fluid expulsion sites on the Cascadia accretionary prism: Mapping diagenetic deposits with processed GLORIA imagery. *Journal of Geophysical Research*, *99*(B6), 11,959–11,969. https://doi.org/10.1029/94JB00120

Charlou, J. L., Donval, J. P., Fouquet, Y., Ondreas, H., Knoery, J., Cochonat, P., et al. (2004). Physical and chemical characterization of gas hydrates and associated methane plumes in the Congo-Angola Basin. *Chemical Geology*, *205*(3–4), 405–425. https://doi.org/10.1016/j.chemgeo.2003.12.033

Chen, Y., Ussler, W. III, Haflidason, H., Lepland, A., Rise, L., Hovland, M., & Hjelstuen, B. O. (2010). Sources of methane inferred from pore-water δ^{13}C of dissolved inorganic carbon in Pockmark G11, offshore Mid-Norway. *Chemical Geology*, *275*(3–4), 127–138. https://doi.org/10.1016/S0304-4203(97)00019-4

Clague, D. A., Maher, N., & Paull, C. K. (2001). In C. K. Paull, & W. P. Dillon (Eds.), *High-resolution multibeam survey of Hydrate Ridge, offshore Oregon, in Natural gas hydrates: Occurrence, distribution and detection* (pp. 297–303). Washington, DC: American Geophysical Union Geophysical Monographs. https://doi.org/10.1029/GM124p0297

Corredor, F., Shaw, J. H., & Bilotti, F. (2005). Structural styles in the deep-water fold and thrust belts of the Niger Delta. *AAPG Bulletin*, *89*(6), 753–780. https://doi.org/10.1306/02170504074

Daigle, H., Bangs, N. L., & Dugan, B. (2011). Transient hydraulic fracturing and gas release in methane hydrate settings: A case study from southern Hydrate Ridge. *Geochemistry, Geophysics, Geosystems*, *12*, Q12022. https://doi.org/10.1029/2011GC003841

Daigle, H., & Dugan, B. (2011). Capillary controls on methane hydrate distribution and fracturing in advective systems. *Geochemistry, Geophysics, Geosystems*, *12*, Q01003. https://doi.org/10.1029/2010GC003392

de Prunelé, A., Ruffine, L., Riboulot, V., Peters, C. A., Croguennec, C., Guyader, V., et al. (2017). Focused hydrocarbon-migration in shallow sediments of a pockmark cluster in the Niger Delta (off Nigeria). *Geochemistry, Geophysics, Geosystems*, *18*, 93–112. https://doi.org/10.1002/2016GC006554

Dickens, G. R. (2001). Sulfate profiles and barium fronts in sediment on the Blake Ridge: Present and past methane fluxes through a large gas hydrate reservoir. *Geochimica et Cosmochimica Acta*, *65*(4), 529–543. https://doi.org/10.1016/S0016-7037(00)00556-1

Duan, Z., & Mao, S. (2006). A thermodynamic model for calculating methane solubility, density and gas phase composition of methane-bearing aqueous fluids from 273 to 523 K and from 1 to 2000 bar. *Geochimica et Cosmochimica Acta*, *70*(13), 3369–3386. https://doi.org/10.1016/j.gca.2006.03.018

Fischer, D., Mogollón, J. M., Strasser, M., Pape, T., Bohrmann, G., Fekete, N., et al. (2013). Subduction zone earthquake as potential trigger of submarine hydrocarbon seepage. *Nature Geoscience*, *6*(8), 647–651. https://doi.org/10.1038/ngeo1886

Fleming, K., Johnston, P., Zwartz, D., Yokoyama, Y., Lambeck, K., & Chappell, J. (1998). Refining the eustatic sea-level curve since the Last Glacial Maximum using far- and intermediate-field sites. *Earth and Planetary Science Letters*, *163*(1–4), 327–342. https://doi.org/10.1016/S0012-821X(98)00198-8

Flemings, P. B., Liu, X., & Winters, W. J. (2003). Critical pressure and multiphase flow in Blake Ridge gas hydrates. *Geology*, *31*(12), 1057–1060. https://doi.org/10.1130/G19863.1

Fontanier, C., Koho, K. A., Goñi-Urriza, M. S., Deflandre, B., Galaup, S., Ivanovsky, A., et al. (2014). Benthic foraminifera from the deep-water Niger delta (Gulf of Guinea): Assessing present-day and past activity of hydrate pockmarks. *Deep Sea Research Part I*, *94*, 87–106. https://doi.org/10.1016/j.dsr.2014.08.011

Freudenthal, T., & Wefer, G. (2013). Drilling cores on the sea floor with the remote-controlled sea floor drilling rig MeBo. *Geoscientific Instrumentation Methods and Data Systems*, *2*(2), 329–337. https://doi.org/10.5194/gi-2-329-2013

Gay, A., Lopez, M., Berndt, C., & Seranne, M. (2007). Geological controls on focused fluid flow associated with seafloor seeps in the Lower Congo Basin. *Marine Geology*, *244*(1–4), 68–92. https://doi.org/10.1016/j.margeo.2007.06.003

George, R. A., & Cauquil, E. (2007). *AUV ultrahigh-resolution 3D seismic technique for detailed subsurface investigations, paper presented at Offshore Technology Conference*. Texas: Houston.

Haeckel, M., Suess, E., Wallmann, K., & Rickert, D. (2004). Rising methane gas bubbles form massive hydrate layers at the seafloor. *Geochimica et Cosmochimica Acta*, *68*(21), 4335–4345. https://doi.org/10.1016/j.gca.2004.01.018

Heeschen, K. U., Hohnberg, H. J., Haeckel, M., Abegg, F., Drews, M., & Bohrmann, G. (2007). In situ hydrocarbon concentrations from pressurized cores in surface sediments, Northern Gulf of Mexico. *Marine Chemistry*, *107*(4), 498–515. https://doi.org/10.1016/j.marchem.2007.08.008

Hensen, C., Zabel, M., Pfeifer, K., Schwenk, T., Kasten, S., Riedinger, N., et al. (2003). Controls of sulfate pore-water profiles by sedimentary events and the significance of anaerobic oxidation of methane for the burial of sulfur in marine sediments. *Geochimica et Cosmochimica Acta*, *67*(14), 2631–2647. https://doi.org/10.1016/S0016-7037(00)00199-6

Hesse, R. (2003). Pore water anomalies of submarine gas-hydrate zones as tool to assess hydrate abundance and distribution in the subsurface: What have we learned in the past decade? *Earth-Science Reviews*, *61*(1–2), 149–179. https://doi.org/10.1016/s0012-8252(02)00117-4

Hoehler, T. M., Alperin, M. J., Albert, D. B., & Martens, C. S. (1994). Field and laboratory studies of methane oxidation in an anoxic marine sediment: Evidence for a methanogen-sulfate reducer consortium. *Global Biogeochemical Cycles*, *8*(4), 451–463. https://doi.org/10.1029/94GB01800

Hong, W.-L., & Peszynska, M. (2018). Geochemical aspects. In L. Ruffine, D. Broseta, & A. Desmedt (Eds.), *Gas Hydrates 2—Geoscience issues and potential industrial applications* (pp. 219–241). Inc: John Wiley & Sons. https://doi.org/10.1002/9781119451174.ch11

Hong, W.-L., Torres, M. E., Carroll, J., Crémière, A., Panieri, G., Yao, H., & Serov, P. (2017). Seepage from an arctic shallow marine gas hydrate reservoir is insensitive to momentary ocean warming. *Nature Communications*, *8*(1), 15745. https://doi.org/10.1038/ncomms15745

Hong, W.-L., Torres, M. E., Portnov, A., Waage, M., Haley, B., & Lepland, A. (2018). Variations in gas and water pulses at an Arctic seep: Fluid sources and methane transport. *Geophysical Research Letters*, *45*, 4153–4162. https://doi.org/10.1029/2018GL077309

Hunt, J. M. (1996). *Petroleum geochemistry and geology* (2nd ed. p. 743). New York: W.H. Freeman.

Judd, A., & Hovland, M. (2007). *Seabed fluid flow. The impact on geology, biology, and the marine environment* (p. 492). Cambridge: Cambridge University Press.

Kannberg, P. K., Tréhu, A. M., Pierce, S. D., Paull, C. K., & Caress, D. W. (2013). Temporal variation of methane flares in the ocean above Hydrate Ridge, Oregon. *Earth and Planetary Science Letters*, *368*, 33–42. https://doi.org/10.1016/j.epsl.2013.02.030

Kelley, J. T., Dickson, S. M., Belknap, D. F., Barnhardt, W. A., & Henderson, M. (1994). Giant sea-bed pockmarks: Evidence for gas escape from Belfast Bay, Maine. *Geology*, *22*(1), 59–62. https://doi.org/10.1130/0091-7613(1994)022<0059:gsbpef>2.3.co;2

Ker, S., Marsset, B., Garziglia, S., Le Gonidec, Y., Gibert, D., Voisset, M., & Adamy, J. (2010). High-resolution seismic imaging in deep sea from a joint deep-towed/OBH reflection experiment: Application to a Mass Transport Complex offshore Nigeria. *GeoJI*, *182*(3), 1524–1542. https://doi.org/10.1111/j.1365-246X.2010.04700.x

Koch, S., Berndt, C., Bialas, J., Haeckel, M., Crutchley, G., Papenberg, C., et al. (2015). Gas-controlled seafloor doming. *Geology*, *43*(7), 571–574. https://doi.org/10.1130/G36596

Kvenvolden, K. A., & McDonald, T. J. (1986). Organic geochemistry on the Joides resolution: An assay, *Technical Note*: Texas A&M Univ, College Station. *Tex. (Ocean Drilling Program)*, *147*.

Liu, J., Haeckel, M., Rutqvist, J., Wang, S., & Yan, W. (2019). The mechanism of methane gas migration through the gas hydrate stability zone: Insights from numerical simulations. *Journal of Geophysical Research: Solid Earth*, *124*, 4399–4427. https://doi.org/10.1029/2019JB017417

Liu, X., & Flemings, P. B. (2007). Dynamic multiphase flow model of hydrate formation in marine sediments. *Journal of Geophysical Research*, *112*, B03101. https://doi.org/10.1029/2005JB004227

Luo, M., Dale, A. W., Wallmann, K., Hensen, C., Gieskes, J., Yan, W., & Chen, D. (2015). Estimating the time of pockmark formation in the SW Xisha Uplift (South China Sea) using reaction-transport modeling. *Marine Geology*, *364*, 21–31. https://doi.org/10.1016/j.margeo.2015.03.006

MacDonald, I. R., Guinasso, N. L., Sassen, R., Brooks, J. M., Lee, L., & Scott, K. T. (1994). Gas hydrate that breaches the sea floor on the continental slope of the Gulf of Mexico. *Geology*, *22*(8), 699–702. https://doi.org/10.1130/0091-7613(1994)022<0699:ghtbts>2.3.co;2

Marcon, Y., Ondréas, H., Sahling, H., Bohrmann, G., & Olu, K. (2014). Fluid flow regimes and growth of a giant pockmark. *Geology*, *42*(1), 63–66. https://doi.org/10.1130/g34801.1

Marsset, T., Marsset, B., Ker, S., Thomas, Y., & Le Gall, Y. (2010). High and very high resolution deep-towed seismic system: Performance and examples from deep water Geohazard studies. *Deep Sea Research Part I*, *57*(4), 628–637. https://doi.org/10.1016/j.dsr.2010.01.001

Marsset, T., Ruffine, L., Gay, A., Ker, S., & Cauquil, E. (2018). Types of fluid-related features controlled by sedimentary cycles and fault network in deepwater Nigeria. *Marine and Petroleum Geology*, *89*, 330–349. https://doi.org/10.1016/j.marpetgeo.2017.10.004

Milkov, A. V. (2011). Worldwide distribution and significance of secondary microbial methane formed during petroleum biodegradation in conventional reservoirs. *Organic Geochemistry*, *42*(2), 184–207. https://doi.org/10.1016/j.orggeochem.2010.12.003

Milkov, A. V., & Etiope, G. (2018). Revised genetic diagrams for natural gases based on a global dataset of >20,000 samples. *Organic Geochemistry*, *125*, 109–120. https://doi.org/10.1016/j.orggeochem.2018.09.002

Nimblett, J., & Ruppel, C. (2003). Permeability evolution during the formation of gas hydrates in marine sediments. *Journal of Geophysical Research*, *108*(B9), 2420. https://doi.org/10.1029/2001JB001650

O'Regan, M., Forwick, M., Jakobsson, M., Moran, K., & Mosher, D. (2015). Seafloor cratering and sediment remolding at sites of fluid escape. *Geology*, *43*(10), 895–898. https://doi.org/10.1130/g36945.1

Orcutt, B. N., Bergenthal, M., Freudenthal, T., Smith, D., Lilley, M. D., Schnieders, L., et al. (2017). Contamination tracer testing with seabed drills: IODP Expedition 357. *Scientific Drilling*, *23*, 39–46. https://doi.org/10.5194/sd-23-39-2017

Paganoni, M., Cartwright, J. A., Foschi, M., Shipp, R. C., & Van Rensbergen, P. (2016). Structure II gas hydrates found below the bottom-simulating reflector. *Geophysical Research Letters*, *43*, 5696–5706. https://doi.org/10.1002/2016GL069452

Panieri, G., Bünz, S., Fornari, D. J., Escartin, J., Serov, P., Jansson, P., et al. (2017). An integrated view of the methane system in the pockmarks at Vestnesa Ridge, 79°N. *Marine Geology*, *390*, 282–300. https://doi.org/10.1016/j.margeo.2017.06.006

Pape, T., Bahr, A., Klapp, S. A., Abegg, F., & Bohrmann, G. (2011a). High-intensity gas seepage causes rafting of shallow gas hydrates in the southeastern Black Sea. *Earth and Planetary Science Letters*, *307*(1–2), 35–46. https://doi.org/10.1016/j.epsl.2011.04.030

Pape, T., Bahr, A., Rethemeyer, J., Kessler, J. D., Sahling, H., Hinrichs, K. U., et al. (2010). Molecular and isotopic partitioning of low-molecular weight hydrocarbons during migration and gas hydrate precipitation in deposits of a high-flux seepage site. *Chemical Geology*, *269*(3–4), 350–363. https://doi.org/10.1016/j.chemgeo.2009.10.009

Pape, T., & Bohrmann, G. (2020). Methane concentration, pore water sulfate and chloride concentrations, and hydrocarbon composition of samples from the Gulf of Guinea. *PANGAEA*. https://doi.org/10.1594/PANGAEA.912516

Pape, T., Bünz, S., Hong, W.-L., Torres, M. E., Riedel, M., Panieri, G., et al. (2020). Origin and transformation of light hydrocarbons ascending at an active pockmark on Vestnesa Ridge, Arctic Ocean. *Journal of Geophysical Research: Solid Earth*, *125*, e2018JB016679. https://doi.org/10.1029/2018JB016679

Pape, T., Feseker, T., Kasten, S., Fischer, D., & Bohrmann, G. (2011b). Distribution and abundance of gas hydrates in near-surface deposits of the Håkon Mosby Mud Volcano, SW Barents Sea. *Geochemistry, Geophysics, Geosystems*, *12*, Q09009. https://doi.org/10.1029/2011GC003575

Pape, T., Geprägs, P., Hammerschmidt, S., Wintersteller, P., Wei, J., Fleischmann, T., et al. (2014). Hydrocarbon seepage and its sources at mud volcanoes of the Kumano forearc basin, Nankai Trough subduction zone. *Geochemistry, Geophysics, Geosystems*, *15*, 2180–2194. https://doi.org/10.1002/2013GC005057

Pau, M., Hammer, Ø., & Chand, S. (2014). Constraints on the dynamics of pockmarks in the SW Barents Sea: Evidence from gravity coring and high-resolution, shallow seismic profiles. *Marine Geology*, *355*, 330–345. https://doi.org/10.1016/j.margeo.2014.06.009

Paull, C. K., Ussler, W. III, Borowski, W. S., & Spiess, F. N. (1995). Methane-rich plumes on the Carolina continental rise: Associations with gas hydrates. *Geology*, *23*(1), 89–92. https://doi.org/10.1130/0091-7613(1995)023<0089:MRPOTC>2.3.CO;2

Peszynska, M., Hong, W.-L., Torres, M. E., & Kim, J.-H. (2016). Methane hydrate formation in Ulleung Basin under conditions of variable salinity: Reduced model and experiments. *Transport in Porous Media*, *114*(1), 1–27. https://doi.org/10.1007/s11242-016-0706-y

Prinzhofer, A., & Pernaton, E. (1997). Isotopically light methane in natural gas: Bacterial imprint or diffusive fractionation? *Chemical Geology*, *142*(3–4), 193–200. https://doi.org/10.1016/S0009-2541(97)00082-X

Quigley, T. M., & Mackenzie, A. S. (1988). The temperatures of oil and gas formation in the sub-surface. *Nature*, *333*(6173), 549–552. https://doi.org/10.1038/333549a0

Reeburgh, W. S. (1976). Methane consumption in Cariaco Trench waters and sediments. *Earth and Planetary Science Letters*, *28*(3), 337–344. https://doi.org/10.1016/0012-821X(76)90195-3

Riboulot, V., Sultan, N., Imbert, P., & Ker, S. (2016). Initiation of gas-hydrate pockmark in deep-water Nigeria: Geo-mechanical analysis and modelling. *Earth and Planetary Science Letters*, *434*, 252–263. https://doi.org/10.1016/j.epsl.2015.11.047

Rohling, E. J., Fenton, M., Jorissen, F. J., Bertrand, P., Ganssen, G., & Caulet, J. P. (1998). Magnitudes of sea-level lowstands of the past 500,000 years. *Nature*, *394*(6689), 162–165. https://doi.org/10.1038/28134

Römer, M., Sahling, H., Pape, T., Bahr, A., Feseker, T., Wintersteller, P., & Bohrmann, G. (2012). Geological control and magnitude of methane ebullition from a high-flux seep area in the Black Sea—The Kerch seep area. *Marine Geology*, *319–322*, 57–74. https://doi.org/10.1016/j.margeo.2012.07.005

Rouby, D., Nalpas, T., Jermannaud, P., Robin, C., Guillocheau, F., & Raillard, S. (2011). Gravity driven deformation controlled by the migration of the delta front: The Plio-Pleistocene of the Eastern Niger Delta. *Tectonophysics*, *513*(1–4), 54–67. https://doi.org/10.1016/j.tecto.2011.09.026

Ruffine, L., Caprais, J.-C., Bayon, G., Riboulot, V., Donval, J.-P., Etoubleau, J., et al. (2013). Investigation on the geochemical dynamics of a hydrate-bearing pockmark in the Niger Delta. *Marine and Petroleum Geology*, *43*, 297–309. https://doi.org/10.1016/j.marpetgeo.2013.01.008

Sahling, H., Bohrmann, G., Spiess, V., Bialas, J., Breitzke, M., Ivanov, M., et al. (2008). Pockmarks in the Northern Congo Fan area, SW Africa: Complex seafloor features shaped by fluid flow. *Marine Geology*, *249*(3–4), 206–225. https://doi.org/10.1016/j.margeo.2007.11.010

Schoell, M. (1983). Genetic characterization of natural gases. *AAPG Bulletin*, *67*(12), 2225–2238. https://doi.org/10.1306/AD46094A-16F7-11D7-8645000102C1865D

Seeberg-Elverfeldt, J., Schlüter, M., Feseker, T., & Kölling, M. (2005). Rhizon sampling of porewaters near the sediment-water interface of aquatic systems. *Limnology and Oceanography, Methods*, *3*(8), 361–371. https://doi.org/10.4319/lom.2005.3.361

Serié, C., Huuse, M., & Schødt, N. H. (2012). Gas hydrate pingoes: Deep seafloor evidence of focused fluid flow on continental margins. *Geology*, *40*(3), 207–210. https://doi.org/10.1130/g32690.1

Simonetti, A., Knapp, J. H., Sleeper, K., Lutken, C. B., Macelloni, L., & Knapp, C. C. (2013). Spatial distribution of gas hydrates from high-resolution seismic and core data, Woolsey Mound, Northern Gulf of Mexico. *Marine and Petroleum Geology*, *44*, 21–33. https://doi.org/10.1016/j.marpetgeo.2013.04.004

Sloan, E. D., & Koh, C. A. (2007). *Clathrate hydrates of natural gases*. Boca Raton: CRC press.

Snyder, G. T., Sano, Y., Takahata, N., Matsumoto, R., Kakizaki, Y., & Tomaru, H. (2020). Magmatic fluids play a role in the development of active gas chimneys and massive gas hydrates in the Japan Sea. *Chemical Geology*, *535*, 119462. https://doi.org/10.1016/j.chemgeo.2020.119462

Suess, E., Torres, M., Bohrmann, G., Collier, R. W., Rickert, D., Goldfinger, C., et al. (2001). Sea floor methane hydrates at Hydrate Ridge, Cascadia Margin. In C. K. Paull, & W. P. Dillon (Eds.), *Natural gas hydrates—Occurrences, distribution and detection* (pp. 87–98). Washington D.C.: American Geophysical Union.

Sultan, N., Bohrmann, G., Ruffine, L., Pape, T., Riboulot, V., Colliat, J.-L., et al. (2014). Pockmark formation and evolution in deepwater Nigeria: Rapid hydrate growth versus slow hydrate dissolution. *Journal of Geophysical Research: Solid Earth*, *119*, 2679–2694. https://doi.org/10.1002/2013JB010546

Sultan, N., Garziglia, S., & Ruffine, L. (2016). New insights into the transport processes controlling the sulfate-methane-transition-zone near methane vents. *Scientific Reports*, *6*(1), 26701. https://doi.org/10.1038/srep26701

Sultan, N., Marsset, B., Ker, S., Marsset, T., Voisset, M., Vernant, A. M., et al. (2010). Hydrate dissolution as a potential mechanism for pockmark formation in the Niger delta. *Journal of Geophysical Research*, *115*, B08101. https://doi.org/10.1029/2010JB007453

Sun, R., & Duan, Z. (2007). An accurate model to predict the thermodynamic stability of methane hydrate and methane solubility in marine environments. *Chemical Geology*, *244*(1–2), 248–262. https://doi.org/10.1016/j.chemgeo.2007.06.021

Taleb, F., Garziglia, S., & Sultan, N. (2018). Hydromechanical properties of gas hydrate-bearing fine sediments from in situ testing. *Journal of Geophysical Research: Solid. Earth*, *123*, 9615–9634. https://doi.org/10.1029/2018JB015824

Taleb, F., Lemaire, M., Garziglia, S., Marsset, T., & Sultan, N. (2020). Seafloor depressions on the Nigerian margin: Seabed morphology and sub-seabed hydrate distribution. *Marine and Petroleum Geology*, *114*, 104175. https://doi.org/10.1016/j.marpetgeo.2019.104175

Tishchenko, P., Hensen, C., Wallmann, K., & Wong, C. S. (2005). Calculation of the stability and solubility of methane hydrate in seawater. *Chemical Geology*, *219*(1–4), 37–52. https://doi.org/10.1016/j.chemgeo.2005.02.008

Tissot, B. P., & Welte, D. H. (1984). *Petroleum formation and occurrence* (2nd ed.). Berlin Heidelberg: Springer-Verlag.

Torres, M. E., Kim, J.-H., Choi, J.-Y., Ryu, B.-J., Bahk, J.-J., Riedel, M., et al. (2011). *Occurrence of high salinity fluids associated with massive near-seafloor gas hydrate deposits, paper presented at 7th International Conference on Gas Hydrates*. Scotland, United Kingdom: Edinburgh.

Torres, M. E., Wallmann, K., Tréhu, A. M., Bohrmann, G., Borowski, W. S., & Tomaru, H. (2004). Gas hydrate growth, methane transport, and chloride enrichment at the southern summit of Hydrate Ridge, Cascadia margin off Oregon. *Earth and Planetary Science Letters*, *226*(1–2), 225–241. https://doi.org/10.1016/j.epsl.2004.07.029

Tréhu, A. M., Long, P. E., Torres, M. E., Bohrmann, G., Rack, F. R., Collett, T. S., et al. (2004). Three-dimensional distribution of gas hydrate beneath southern Hydrate Ridge: Constraints from ODP Leg 204. *Earth and Planetary Science Letters*, *222*(3–4), 845–862. https://doi.org/10.1016/j.epsl.2004.03.035

Tryon, M. D., Brown, K. M., Torres, M. E., Tréhu, A. M., McManus, J., & Collier, R. W. (1999). Measurements of transience and downward fluid flow near episodic methane gas vents, Hydrate Ridge, Cascadia. *Geology*, *27*(12), 1075–1078. https://doi.org/10.1130/0091-7613(1999)027<1075:MOTADF>2.3.CO;2

Ussler, W. III, & Paull, C. K. (1995). Effects of ion exclusion and isotopic fractionation on pore water geochemistry during gas hydrate formation and decomposition. *Geo-Marine Letters*, *15*(1), 37–44. https://doi.org/10.1007/BF01204496

Ussler, W. III, & Paull, C. K. (2001). In C. K. Paull, & W. P. Dillon (Eds.), *ion exclusion associated with marine gas hydrate deposits, in Natural gas hydrates: Occurrence, distribution and detection* (pp. 41–52). Washington, DC: American Geophysical Union.

Valentine, D. L. (2011). Emerging topics in marine methane biogeochemistry. *Annual Review of Marine Science*, *3*(1), 147–171. https://doi.org/10.1146/annurev-marine-120709-142734

Waelbroeck, C., Labeyrie, L., Michel, E., Duplessy, J. C., McManus, J. F., Lambeck, K., et al. (2002). Sea-level and deep water temperature changes derived from benthic foraminifera isotopic records. *Quaternary Science Reviews*, *21*(1–3), 295–305. https://doi.org/10.1016/S0277-3791(01)00101-9

Waite, W. F., Stern, L. A., Kirby, S. H., Winters, W. J., & Mason, D. H. (2007). Simultaneous determination of thermal conductivity, thermal diffusivity and specific heat in sI methane hydrate. *GeoJI*, *169*(2), 767–774. https://doi.org/10.1111/j.1365-246X.2007.03382.x

Wallmann, K., Riedel, M., Hong, W.-L., Patton, H., Hubbard, A., Pape, T., et al. (2018). Gas hydrate dissociation off Svalbard induced by isostatic rebound rather than global warming. *Nature Communications*, *9*(1), 83. https://doi.org/10.1038/s41467-017-02550-9

Wei, J., Pape, T., Sultan, N., Colliat, J.-L., Himmler, T., Ruffine, L., et al. (2015). Gas hydrate distributions in sediments of pockmarks from the Nigerian margin—Results and interpretation from shallow drilling. *Marine and Petroleum Geology*, *59*, 359–370. https://doi.org/10.1016/j.marpetgeo.2014.09.013

Wenau, S., Spieß, V., Pape, T., & Fekete, N. (2017). Controlling mechanisms of giant deep water pockmarks in the Lower Congo Basin. *Marine and Petroleum Geology*, *83*, 140–157. https://doi.org/10.1016/j.marpetgeo.2017.02.030

Wilhelms, A., Larter, S. R., Head, I., Farrimond, P., di Primio, R., & Zwach, C. (2001). Biodegradation of oil in uplifted basins prevented by deep-burial sterilization. *Nature*, *411*(6841), 1034–1037. https://doi.org/10.1038/35082535

Wood, W. T., Gettrust, J. F., Chapman, N. R., Spence, G. D., & Hyndman, R. D. (2002). Decreased stability of methane hydrates in marine sediments owing to phase-boundary roughness. *Nature*, *420*(6916), 656–660. https://doi.org/10.1038/nature01263

Zander, T., Haeckel, M., Klaucke, I., Bialas, J., Klaeschen, D., Papenberg, C., et al. (2020). New insights into geology and geochemistry of the Kerch seep area in the Black Sea. *Marine and Petroleum Geology*, *113*, 104162. https://doi.org/10.1016/j.marpetgeo.2019.104162

References From the Supporting Information

Davidson, D. W. (1981). Gas hydrates as clathrates ices. In J. L. Cox (Ed.), *Natural gas hydrates: Properties, occurrence, and recovery* (pp. 1–15). Boston: Butterworth.

Koh, C. A. (2002). Towards a fundamental understanding of natural gas hydrates. *Chemical Society Reviews*, *31*(3), 157–167. https://doi.org/10.1039/B008672J

Riboulot, V., Cattaneo, A., Berné, S., Schneider, R. R., Voisset, M., Imbert, P., & Grimaud, S. (2012). Geometry and chronology of late Quaternary depositional sequences in the Eastern Niger Submarine Delta. *Marine Geology*, *319–322*, 1–20. https://doi.org/10.1016/j.margeo.2012.03.002

Spinelli, G. A., Giambalvo, E. R., & Fisher, A. T. (2004). Sediment permeability, distribution, and influence on fluxes in oceanic basement. In A. T. Fisher, E. E. Davis & H. Elderfield (Eds.), *Hydrogeology of the oceanic lithosphere* (pp. 151–188). Cambridge, UK: Cambridge University Press.

Wefer, G., Berger, W. H., Richter, C., et al. (1988). Proceedings of the Ocean Drilling Program, initial reports, College Station, Texas (Ocean Drilling Program). https://doi.org/10.2973/odp.proc.ir.175.1998